

Numerical study of turbulent channel flow perturbed by spanwise topographic heterogeneity: Amplitude and frequency modulation within low- and high-momentum pathways

Ankit Awasthi and William Anderson*

Mechanical Engineering Department, The University of Texas at Dallas, Richardson, Texas 75080, USA



(Received 5 February 2018; published 9 April 2018)

We have studied the effects of topographically driven secondary flows on inner-outer interaction in turbulent channel flow. Recent studies have revealed that large-scale motions in the logarithmic region impose an amplitude and frequency modulation on the dynamics of small-scale structures near the wall. This led to development of a predictive model for near-wall dynamics, which has practical relevance for large-eddy simulations. Existing work on amplitude modulation has focused on smooth-wall flows; however, Anderson [*J. Fluid Mech.* **789**, 567 (2016)] addressed the problem of rough-wall turbulent channel flow in which the correlation profiles for amplitude modulation showed trends similar to those reported by Mathis *et al.* [*Phys. Fluids* **21**, 111703 (2009)]. For the present study, we considered flow over surfaces with a prominent spanwise heterogeneity, such that domain-scale turbulent secondary flows in the form of counter-rotating vortices are sustained within the flow. (We also show results for flow over a homogeneous roughness, which serves as a benchmark against the spanwise-perturbed cases.) The vortices are anchored to the topography such that prominent upwelling and downwelling occur above the low and high roughness, respectively. We have quantified the extent to which such secondary flows disrupt the distribution of spectral density across constituent wavelengths throughout the depth of the flow, which has direct implications for the existence of amplitude and frequency modulation. We find that the distinct outer peak associated with large-scale motions—the “modulators”—is preserved within the upwelling zone but vanishes in the downwelling zone. Within the downwelling zones, structures are steeper and shorter. Single- and two-point correlations for inner-outer amplitude and frequency modulation demonstrate insensitivity to resolution across cases. We also show a pronounced crossover between the single- and two-point correlations, a product of modulation quantification based upon Parseval’s theorem (i.e., spectral density, but not the wavelength at which energy resides, defines the strength of modulation).

DOI: [10.1103/PhysRevFluids.3.044602](https://doi.org/10.1103/PhysRevFluids.3.044602)

I. INTRODUCTION

Near-wall turbulence is an important area of study due to its ubiquity in various flow conditions in the environment and engineering applications. Turbulent structures get smaller as the wall is approached [1], which makes laboratory measurement difficult and presents resolution challenges for numerical simulations. These challenges become more pronounced with increasing Reynolds number. There have been extensive studies on flow over smooth walls, which have revealed the presence of coherent structures of different scales, ranging from those associated with the near-wall cycle [2–5] to large-scale motions (LSMs) [6,7] encapsulated by hairpin vortices [8,9] within the

*Corresponding author: wca140030@utdallas.edu

logarithmic region. Roughness ablates the viscous near-wall region (inner cycle) by the formation of roughness-scale eddies [10–12], resulting in the roughness sublayer [13,14]. The ratio of flow depth, H , to aggregate element height, h , is widely used as an indicator of the outer (inertial) layer flow state. For $H/h \gtrsim 30$, roughness serves to impose a momentum deficit, ΔU^+ , without any structural modification to outer-layer flow structures [1]. Outer-layer similarity has been confirmed by various experiments [7,15–17]; however, some have reported roughness effects on the streamwise velocity fluctuations in the outer layer [18] (in this article, the first, second, and third component of any vector corresponds with its magnitude in the streamwise, spanwise, and wall-normal direction, respectively, and we adopt $\mathbf{x} = \{x, y, z\}$ for spatial position). LSMs are zones of quasiuniform momentum deficit or excess (low- or high-momentum regions), with streamwise extent, l_1 , comparable to the flow depth, where $l_1/H \approx 3$ is commonly observed. LSMs exhibit a streamwise inclination angle, $\theta \approx 17^\circ$, which provides a basis for their length since $H/\tan \theta \approx 3H = l_1$. Individual LSMs generally undergo a quasistreamwise coalescence [19–22], resulting in spatially meandering very-large-scale motions (VLSMs) [7] with streamwise extent, $l_2/H \approx 21$. The existence of VLSMs has been well documented in pipes [23,24], channels [25,26], and boundary layers [15,17,27].

The “signature” of VLSMs is readily discerned from pre-multiplied energy spectra (spectrograms) [7,25,26]. The near-wall region, whether occupied by a roughness or viscous sublayer, features a prominent peak in spectral density that diminishes with magnitude in the wall-normal direction. In order to resolve VLSMs, two conditions are simultaneously required: (1) the test section (i.e., laboratory length or computation domain streamwise extent) must at least exceed l_2 , and (2) the roughness Reynolds number, $\text{Re}_\tau = u_\tau H/\nu$, where u_τ is shear velocity and ν is kinematic viscosity, must be $\text{Re}_\tau \gtrsim 2000$ [7]. When these conditions are simultaneously attained, spectrograms will exhibit a second peak within the logarithmic region and residing at wavelength equivalent to the length of VLSMs. In recent times, the simultaneous coexistence of outer- and inner-layer structures—where “inner” is used here in a broad sense to encompass both the inner cycle for smooth walls and the roughness sublayer for rough walls—has received significant attention [28–32]. Experimental measurement of smooth-wall turbulent boundary layers has revealed a distinct modulation of the amplitude [28,29] and frequency of inner-layer velocity fluctuations [33–35], while more recent studies have demonstrated an analogous amplitude modulation of the roughness sublayer by outer-layer LSMs [35–37].

Mathis *et al.* [29] used the Hilbert transform of the low-pass-filtered velocity fluctuations to compute the degree of small-scale amplitude modulation by ambient large-scale features. They concluded that large-scale structures appeared to amplitude-modulate the small-scale fluctuations and showed that during an event of large-scale momentum deficit there are reduced small-scale fluctuations in the near-wall regions, whereas during a large-scale momentum excess event the small-scale fluctuations are enhanced. And this phenomenon is reversed away from the wall, since the small-scale fluctuations tend to align themselves with the large-scale momentum deficit region [29]. These studies on inner-outer interactions led to the development of a predictive model for near-wall dynamics [30]. In this model, Mathis *et al.* [30] used empirically determined parameters to predict the statistics of small-scale velocity fluctuations near the wall. Anderson [36] followed the approach outlined by Mathis *et al.* [29] for atmospheric boundary-layer-like flow over an array of wall-mounted blocks. This study demonstrated an analogous modulation of roughness sublayer amplitude with the passage of outer-layer LSMs.

Most preceding studies on inner-outer interaction have been devoted to smooth walls or idealized roughness (homogeneous sandpaper or distributions of elements composed of a few scales). Such canonical arrangements are, of course, the exception in realistic engineering and geophysical flows. In this article, we highlight how one particular surface complexity—spanwise heterogeneity—disrupts the coexisting inner-outer structural paradigm, and we characterize the implications of this for large-scale modulation of small-scale amplitude and frequency. To this extent, we stress a complementary article by Pathikonda and Christensen [35], who performed an experimental assessment of the roughness-induced changes on amplitude and frequency modulation. They concluded that even though the correlation profiles are similar to those for smooth walls, amplitude and frequency

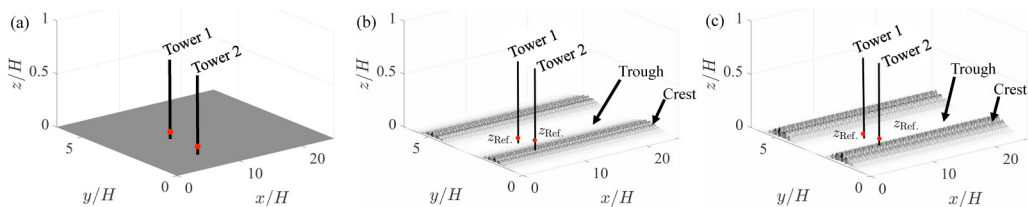


FIG. 1. Illustration of the topographies considered in present study: (a) case 1, (b) case 2, and (c) case 3 (cases 4 and 7 are higher-resolution versions of case 1, and so on, which precludes the need to provide images of the additional cases). The panels include annotation of the reference heights, z_{Ref} , needed to compute correlations for amplitude and frequency modulation. The panels also include annotation of virtual towers over which time-series measurements of fluctuating velocity was recorded (in (a), we say simply “Tower 1” and “Tower 2,” since this case is a homogeneous roughness without any “Trough” or “Crest”). Table I contains additional simulation attributes.

modulation is more intense in rough-wall flows (this observation is also consistent with amplitude modulation observations by Anderson [36]). This increased correlation was shown to be due to Reynolds-averaged secondary motions sustained by the surface heterogeneity. For this work, we perform a similar study, but applied to a limiting topographic arrangement which features the salient characteristics of spanwise heterogeneity, absent small-scale topographic features that might otherwise diminish the generality of the results.

A. Low- and high-momentum pathways

Recent studies have shown that there is a high degree of spanwise heterogeneity in the Reynolds-averaged flow when the surface roughness features a prominent spanwise heterogeneity [38–46]. This has been confirmed via experiments and numerical simulations, wherein the Reynolds-averaged flow features heterogeneities in the spanwise–wall-normal plane that would otherwise vanish in the absence of spanwise surface heterogeneity. Notably, the Reynolds-averaged streamwise momentum exhibits pronounced spanwise undulations about the mean profile, where momentum excesses and deficits have been labeled high-momentum pathways (HMPs) and low-momentum pathways (LMPs), respectively, by Christensen *et al.* [12,42]. These LMPs and HMPs are flanked by mean secondary cells, such that downwelling and upwelling occur above the regions of “high” and “low” roughness, respectively.

Anderson *et al.* [43] demonstrated that the turbulent secondary flows [47] were a manifestation of Prandtl’s secondary flow of the second kind: driven and sustained by spanwise heterogeneity in components of the Reynolds stresses [48–51]. Other studies have recently explored how spacing between spanwise-adjacent surface heterogeneities affects the flow [45,52], and how such heterogeneities disrupt the structural attributes of low- and high-momentum regions within the flow [44]. Although the application of these concepts to wall turbulence is a relatively recent development, the work itself leverages concepts already explored by the hydraulic engineering community [47,53–55] and turbulent duct flow community [47,48,50,56,57].

For this article, we have explored how topographically driven Reynolds-averaged turbulent secondary flows disrupt the morphology of outer (inertial) layer turbulence, and we have quantified the implications of this for inner-outer interactions. We have used topographies featuring dramatic spanwise heterogeneity, which guarantees the sustenance of turbulent secondary flows and the associated low- and high-momentum pathways. Figure 1 shows the cases considered (two spanwise heterogeneous cases, and a homogeneous roughness case, against which we compare results; discussion to follow in subsequent sections). Spectrograms reveal that the distribution of spectral density is changed substantially by LMPs and HMPs, yet the magnitude of inner-outer correlations still compares reasonably well against canonical flows. The results thus highlight the underlying presence of an inner-outer interaction even under conditions very different from the canonical

wall flows for which the schemes were originally developed. For this work, we have adopted the wavelet-based computation of correlations, following Baars *et al.* [34] and Pathikonda and Christensen [35].

B. Wavelet analysis

Wavelet decomposition allows the content of an input time series to be decomposed in joint time-frequency space, which is particularly helpful for studies such as this where the large scales (low frequency) are regarded as modulators of the small scales (high frequency). Herein, we obtain a time series of streamwise velocity fluctuations by subtracting the Reynolds-averaged velocity from the instantaneous, $\tilde{u}'(x_l, y_l, z, t) = \tilde{u}(x_l, y_l, z, t) - \langle \tilde{u}(x_l, y_l, z, t) \rangle_T$, where $\langle \cdot \rangle_T$ denotes the time average, $\tilde{\cdot}$ denotes a grid-filtered (large-eddy simulation [LES]) quantity, and $\{x_l, y_l\}$ is a discrete local position in the horizontal (x - y) plane at which a virtual tower is placed [58]. A comprehensive description of the LES code is provided below, and we have utilized the LES nomenclature here in order to promote consistency with the latter sections of this paper. Figure 1 illustrates the cases considered in this study, where the virtual towers are annotated by vertical profiles at fixed spanwise locations [note that Fig. 1(a) shows a homogeneous roughness, which serves as a comparison case for other results in this paper). The large-scale component of $\tilde{u}'(x_l, y_l, z, t)$ the component associated with large-scale motions—can be attained via convolution with a low-pass filter, $\tilde{u}'_L(x_l, y_l, z, t) = G_L \star \tilde{u}'(x_l, y_l, z, t)$, where \star denotes convolution and G_L is a filtering kernel with scale, $L = \delta_T U_0 H^{-1} = 2.0$, where U_0 is an “outer” characteristic advective velocity, H is the flow depth, and δ_T is the (dimensional) time associated with the overturning of one domain-scale eddy. In this work, the inner and outer layers are separated by filtering at two large-eddy turnovers, following the precedent already established in preceding studies of smooth- and rough-wall flows [30,36]. Below, we present the techniques used to quantify how $\tilde{u}'_L(x_l, y_l, z, t)$ modulates the amplitude and frequency of the small-scale component, $\tilde{u}'_S(x_l, y_l, z, t) = \tilde{u}'(x_l, y_l, z, t) - \tilde{u}'_L(x_l, y_l, z, t)$. Here, we use Morlet wavelets, which are given by the expression

$$\psi(t/t_s) = e^{i\omega_\psi t/t_s} e^{-|t/t_s|^2/2}, \quad (1)$$

where t_s is the wavelet timescale normalized by the eddy-turnover time ($\delta_T U_0/H$). Joint time-frequency analysis is accomplished via convolution of \tilde{u}' with a spectrum of wavelet functions:

$$\tilde{u}'_*(x_l, y_l, z, t; t_s) = \int_{-\infty}^{\infty} \tilde{u}'(x_l, y_l, z, \tau) \psi\left(\frac{\tau - t}{t_s}\right) d\tau, \quad (2)$$

where $\tilde{u}'_*(x_l, y_l, z, t; t_s)$ is the decomposed fluctuating velocity in time-frequency space. Now, the spectral density is obtained by taking the squared modulus of the coefficients obtained by the convolution:

$$E(z, t, f) = |\tilde{u}'_*(x_l, y_l, z, t; t_s)|^2, \quad (3)$$

where $E(z, t, f)$ is the pre-multiplied wavelet power spectrum (WPS) at a given time, t , and frequency, f , based on the input time series, $\tilde{u}'(x_l, y_l, z, t)$ (for brevity, we exclude the horizontal location from within the WPS field). To obtain the energy content associated with the small-scale energy of the WPS, we use Parseval’s theorem as shown in the work of Baars *et al.* [34]:

$$\sigma_S(z, t) = \left[\int_{f_c}^{f_N} E(z, t, f) df \right]^{1/2}, \quad (4)$$

where $\sigma_S(z, t)$ is the instantaneous standard deviation associated with the small scales, f_c corresponds to the separation scale between large- and small-scale velocity fluctuations, and f_N corresponds to the Nyquist frequency, which is half of the sampling frequency, f_S . Herein, we set $f_c = H U_0^{-1} \delta_T^{-1} = L^{-1} = 0.5$; in fact, the choice of f_c had virtually no implications for the resultant measure of

amplitude and frequency modulation, since the inner and outer peaks reside at distinctly different wavelengths. Provided $f_c \approx 1$, the resultant correlations will only differ moderately.

Equation (4) gives the instantaneous standard deviation, which can be decomposed into its (nonzero) mean and fluctuating component: $\sigma_S(z,t) = \sqrt{\langle u'_S(z,t)^2 \rangle_T} + \sigma'_S(z,t)$. The aim of this work is to investigate how large-scale (low-frequency) velocity fluctuations modulate small scales (high frequency). The approach outlined here is ideally suited for such studies, as it simultaneously provides information on the time-varying small- and large-scale energy. In order to obtain the large-scale variation of the small-scale amplitude, we apply the low-pass filter, yielding $\sigma'_{SL}(z,t) = G_L \star \sigma'_S(z,t)$ (this filtering of the small-scale amplitude is a widely used practice [30,34–36] to capture salient features of the small scales). In order to quantify the modulation of small-scale frequency, we construct a time series for instantaneous frequency [59,60] by computing the first spectral moment of the instantaneous WPS:

$$f^*(z,t) = \frac{1}{|\sigma_S(z,t)|^2} \int_{f_c}^{f_N} E(z,t,f) f \log_{10} f d \log_{10} f, \quad (5)$$

where

$$f_S(z,t) = 10^{f^*(z,t)}. \quad (6)$$

We obtain the fluctuating component of the instantaneous frequency by subtracting the mean, $f'_S(z,t) = f_S(z,t) - \langle f_S \rangle_T(z)$, which is then low-pass filtered, $f'_{SL}(z,t) = G_L \star f'_S(z,t)$. Having completed the preceding steps, we can now quantify the extent to which $\tilde{u}'_L(x_l, y_l, z, t)$ modulates the amplitude and frequency of its small-scale counterpart via correlation with $\sigma'_{SL}(z,t)$ and $f'_{SL}(z,t)$, respectively, via

$$R_a(z; z) = \frac{\langle \tilde{u}'_L(z,t) \sigma'_{SL}(z,t) \rangle_T}{\sqrt{\langle \tilde{u}'_L{}^2(z,t) \rangle_T} \sqrt{\langle \sigma'^2_{SL}(z,t) \rangle_T}} \quad (7)$$

and

$$R_f(z; z) = \frac{\langle \tilde{u}'_L(z,t) f'_{SL}(z,t) \rangle_T}{\sqrt{\langle \tilde{u}'_L{}^2(z,t) \rangle_T} \sqrt{\langle f'^2_{SL}(z,t) \rangle_T}}. \quad (8)$$

The correlations, $R_a(z; z)$ and $R_f(z; z)$, quantify the degree of amplitude and frequency modulation, respectively, of the small-scale structures due to large-scale content. The correlations are “single point” (i.e., same elevation), which fails to attain any measure of how large-scale content in the outer layer modulates small-scale content in the inner layer. In order to gain a quantitative description of how large scales in the outer layer—those associated with the outer peak—modulate the amplitude and frequency of small scales in the roughness sublayer, two-point correlations are also computed. That is, we correlate the large scales at a fixed location, $\tilde{u}'_L(z_{\text{Ref.}}, \tau(z; z_{\text{Ref.}}))$, with the small-scale amplitude and frequency over the depth of the flow:

$$R_a(z; z_{\text{Ref.}}) = \frac{\langle \tilde{u}'_L(z_{\text{Ref.}}, \tau(z; z_{\text{Ref.}})) \sigma'_{SL}(z,t) \rangle_T}{\sqrt{\langle \tilde{u}'_L{}^2(z_{\text{Ref.}}, \tau(z; z_{\text{Ref.}})) \rangle_T} \sqrt{\langle \sigma'^2_{SL}(z,t) \rangle_T}} \quad (9)$$

and

$$R_f(z; z_{\text{Ref.}}) = \frac{\langle \tilde{u}'_L(z_{\text{Ref.}}, \tau(z; z_{\text{Ref.}})) f'_{SL}(z,t) \rangle_T}{\sqrt{\langle \tilde{u}'_L{}^2(z_{\text{Ref.}}, \tau(z; z_{\text{Ref.}})) \rangle_T} \sqrt{\langle f'^2_{SL}(z,t) \rangle_T}}. \quad (10)$$

Unlike Eqs. (7) and (8), for which we will use simultaneous input arguments for the large and small scales, for Eqs. (9) and (10) we must impose an advective correction on the large scale (i.e., $\tilde{u}'_L(z_{\text{Ref.}}, t) \rightarrow \tilde{u}'_L(z_{\text{Ref.}}, \tau(z; z_{\text{Ref.}}))$, where $\tau(z; z_{\text{Ref.}}) = t + \lambda(z; z_{\text{Ref.}})$ and $\lambda(z; z_{\text{Ref.}})$ is an advective correction [36,58,61]). $\lambda(z; z_{\text{Ref.}})$ is needed to ensure that two-point correlations are

TABLE I. Summary of large-eddy simulation parameters, where L_x and L_y represent the computational domain streamwise and spanwise extent, respectively, here normalized by the flow depth H . N_x , N_y , and N_z represent the number of grid points in the streamwise, spanwise, and wall-normal directions, respectively; h_{\max} is the maximum height of the topography; and the far-right column, $\delta_T U_0 H^{-1}$, is the number of large-eddy turnovers associated with each simulation.

Case	L_x/H	L_y/H	N_x	N_y	N_z	h_{\max}/H	TU_0/H
1	8π	2π	256	64	64	0	10000
2	8π	2π	256	64	64	0.05	10000
3	8π	2π	256	64	64	0.1	10000
4	8π	2π	384	96	96	0	6500
5	8π	2π	384	96	96	0.05	6500
6	8π	2π	384	96	96	0.1	6500
7	8π	2π	512	128	128	0	2000
8	8π	2π	512	128	128	0.05	2000
9	8π	2π	512	128	128	0.1	2000

correctly made between the modulator—LSMs, which exhibit positive streamwise inclination and, thus, negative temporal inclination [58]—and the corresponding small scales at differing heights. Herein, we compute the advective lag profiles *a posteriori*, which are used to correct the large scales before computation of amplitude and frequency modulation. Figure 1 provides a graphical indication of the reference location, z_{Ref} . (the annotation is only for discussion, and precise values of the reference location are provided later in the article). For this article, we have explored how topographically forced turbulent secondary flows alter the distribution of spectral density in the outer layer and the implications of this for inner-outer interactions using Eqs. (7)–(10).

C. Present study

LES has been used to model turbulent channel flow over a variety of rough lower boundaries. We considered flow over two cases of varying topographic height, as shown in Figs. 1(b) and 1(c). These results were compared against results for turbulent channel flow over a homogeneous roughness, Fig. 1(a), in which drag is modeled via the equilibrium logarithmic law through prescription of an aerodynamic roughness length. Table I summarizes key attributes of the surfaces, including the maximum height. The two-dimensional spanwise heterogeneous topographies were constructed via the outer product of two one-dimensional arrays—one featuring two Gaussian mounds, the other featuring a harmonic distribution. These topographies were then rescaled such that the maximum height, h_{\max} , was varied (see also Table I). For the present simulations, the domain spatial extent $(x, y, z) : 0 \leq x/H \leq 8\pi, 0 \leq y/H \leq 2\pi, 0 \leq z/H \leq 1$, where H is the half-channel depth (quick inspection shows that the domain streamwise extent, $8\pi \approx 24$, is sufficiently long to capture at least the beginning of the outer peak [25,30,36]. The friction Reynolds number, $\text{Re}_\tau = u_\tau H/\nu \sim O(10^6)$, indicating that (1) the simulations were carried out under “fully rough” conditions [13], thereby enabling comparison with literature data sets under dynamic similarity, and (2) the inertial conditions satisfied the criteria required for the existence of VLSMs [7]. The simulations are run at three resolutions, as shown in Table I. So, cases 1, 4, and 7 are the Fig. 1(a) topography, cases 2, 5, and 8 are the Fig. 1(b) topography, and cases 3, 6, and 9 are the Fig. 1(c) topography.

Modeling flow over the same topography, but at different resolution, allowed us to assess how domain discretization affected the resultant turbulence statistics and correlation profiles [36]. The maximum heights for cases 1, 2, and 3 were $h_{\max}/H = 0, 0.05$, and 0.1 , respectively. In Sec. II, we present a summary of the LES code and additional details of the cases (time and spatial discretization, subgrid-scale turbulence closures, numerical procedures, etc.). A series of results is presented in Sec. III, from instantaneous flow visualization to demonstration of topographically driven structural

alterations to the outer flow statistics, which ultimately culminates in vertical profiles of the Eqs. (7)–(10) correlations. We demonstrate resolution invariance of the correlation profiles and that the choice of the reference height, $z_{\text{Ref.}}$, plays a major role in the magnitude of the two-point correlation. Moreover, we find a crossover between the single- and two-point amplitude modulation correlations; thus, at a single elevation, the amplitudes of small-scale processes in the roughness sublayer possess equivalent correlation with the large-scale dynamics at the same elevation, or at an elevation in the outer layer. This result, in particular, provides further evidence for the underlying merit of wall models predicated upon amplitude and frequency modulation. Concluding remarks are made in Sec. IV.

II. LARGE-EDDY SIMULATION

The LES code used in this study solves the three-dimensional, grid-filtered momentum transport equations in rotational form [62,63],

$$\frac{\partial \tilde{\mathbf{u}}}{\partial t} + \frac{1}{2} \nabla (\tilde{\mathbf{u}} \cdot \tilde{\mathbf{u}}) - \tilde{\mathbf{u}} \times \tilde{\boldsymbol{\omega}} = -\frac{1}{\rho} \nabla \tilde{p} - \nabla \cdot \boldsymbol{\tau} + \boldsymbol{\Pi} + \mathbf{f}, \quad (11)$$

where $\boldsymbol{\tau} = \widetilde{\mathbf{u} \otimes \mathbf{u}} - \tilde{\mathbf{u}} \otimes \tilde{\mathbf{u}}$ is the subgrid-scale tensor, $\tilde{\boldsymbol{\omega}} = \nabla \times \tilde{\mathbf{u}}$ is vorticity, \mathbf{f} is a body force term that imposes drag associated with solid obstacles [64,65], $\nabla \tilde{p}$ is the pressure correction, and $\boldsymbol{\Pi} = \{u_\tau^2/H = 1, 0, 0\}$ is an imposed pressure-gradient forcing, where H is the channel half height. This code has been diversely used in various flow conditions [66–74].

The present LES code is used to model turbulent channel flow under “fully rough” inertial conditions [13], $\text{Re}_\tau = u_\tau H/\nu \sim O(10^6)$. In order to maintain a solenoidal velocity field, the divergence of Eq. (11) is computed and the incompressibility condition, $\nabla \cdot \tilde{\mathbf{u}} = 0$, is applied. The resultant pressure Poisson equation is solved with Neumann boundary conditions at the top and bottom of the domain, $\partial \tilde{p}/\partial z|_{z/H=1}$ and $\partial \tilde{p}/\partial z|_{z/H=0}$, respectively. Channel centerline conditions are imposed with zero stress, $\partial \tilde{u}/\partial z|_{z/H=1} = \partial \tilde{v}/\partial z|_{z/H=1}$, and zero penetration, $\tilde{w}(x, y, z/H = 1, t) = 0$. Periodic boundary conditions are imposed on the vertical planes of the domain owing to spectral discretization in the horizontal directions. Surface boundary conditions are implemented via the equilibrium logarithmic law and an immersed boundary method (IBM), depending on the value of $h(x, y)$. For $h(x, y) = 0$, the stress is set as

$$\tau_{xz}^w(x, y, t) = - \left[\frac{\kappa U(x, y, \frac{1}{2} \delta z, t)}{\log(\frac{1}{2} \delta z / z_0)} \right]^2 \frac{\tilde{u}(x, y, \frac{1}{2} \delta z, t)}{U(x, y, \frac{1}{2} \delta z, t)} \quad (12)$$

and

$$\tau_{yz}^w(x, y, t) = - \left[\frac{\kappa U(x, y, \frac{1}{2} \delta z, t)}{\log(\frac{1}{2} \delta z / z_0)} \right]^2 \frac{\tilde{v}(x, y, \frac{1}{2} \delta z, t)}{U(x, y, \frac{1}{2} \delta z, t)}, \quad (13)$$

where $z_0/H = 10^{-3}$ is a prescribed roughness length, and $\tilde{\cdot}$ denotes test filtering [66,75], which is used to suppress numerical contamination due to localized implementation of the equilibrium logarithmic law. For $h(x, y) > 0$, an IBM [65] is used to define \mathbf{f} in Eq. (11), which has been successfully used in similar studies [36,43]. The deviatoric component of $\boldsymbol{\tau}$ is evaluated using the eddy-viscosity modeling approach, $\boldsymbol{\tau} - (1/3)\delta \text{Tr}(\boldsymbol{\tau}) = -2\nu_t \tilde{\mathbf{S}}$, where $\nu_t = (C_s \Delta)^2 |\tilde{\mathbf{S}}|$ is the turbulent viscosity, C_s is the Smagorinsky coefficient [76], Δ is the filter size, $\tilde{\mathbf{S}} = (\nabla \tilde{\mathbf{u}} + \nabla \tilde{\mathbf{u}}^T)/2$ is the resolved strain-rate tensor, and $|\tilde{\mathbf{S}}| = (2\tilde{\mathbf{S}} : \tilde{\mathbf{S}})^{1/2}$ is the magnitude of the resolved strain-rate tensor. C_s is evaluated using the Lagrangian-averaged scale-dependent dynamic model of Bou-Zeid *et al.* [66].

Flow stationarity is ensured by running the simulations for the period $10^3 \leq \delta_T U_0/H \leq 10^4$, where $\delta_T U_0/H$ is considered one large-eddy turnover. This is needed to ensure that a sufficiently large number of structures advect through the domain during the averaging period [36,77]. Table I summarizes the averaging time for all simulations, and one immediately observes that the averaging time decreases with increasing resolution, which is a natural product of the practical difficulties

associated with simulations at higher resolution. The affects of this are readily discernible in the turbulence statistics, wherein the cases with $N_x = 256$ and 384 are in close agreement (cases 1–6), while agreement is not as strong for $N_x = 512$ (cases 7–9). Nonetheless, the agreement is reasonable and indicates that we have appropriately reconciled the need for high resolution with the practical constraints inherent to such simulations.

Equation (11) is integrated in time with nondimensional time step $\delta t^* = \delta t u_\tau H^{-1}$, where $\delta t^* = 9 \times 10^{-5}$, 4.5×10^{-5} , and 4.5×10^{-5} , for cases 1–3, 4–6, and 7–9, respectively. The computational mesh is discretized with $\delta x = L_x/N_x$, $\delta y = L_y/N_y$, and $\delta z = 1/N_z$, respectively.

III. RESULTS

This section is composed of five sections. Section III A provides a sampling of instantaneous and Reynolds-averaged flow visualization, which helps to graphically illustrate how the spatial nature of the flow changes in response to a prominent spanwise heterogeneity. We show qualitative evidence that meandering large-scale motions feature similar structural characteristics within LMPs, with inclination angles of $\theta \approx 15^\circ$, but within HMPs the structures get progressively steeper. Following this, in Sec. III B, we show vertical profiles of Reynolds-averaged quantities from virtual towers above the crest and trough, which further highlights major changes to the flows due to spanwise topographic heterogeneity.

Spatial correlations above the crest and trough are used to confirm that, indeed, the structures undergo steepening above the crest (within HMPs), and this result is used to explain how spectral density is shifted across wavelengths in Sec. III D. Finally, in Sec. III E, we show profiles of single- and two-point correlations for modulation of small-scale amplitude and frequency [based on Eqs. (7)–(10), and accompanying text]. The figures reveal a distinct crossover in the single- and two-point correlations, which is a unique result. This result is a consequent of Parseval’s theorem: since our description of amplitude modulation is predicated upon the spectral density associated with the small scales, but not the wavelength at which the spectral density resides, correlation crossovers are entirely possible.

Throughout this section, results are cited as being retrieved from a virtual tower above the crest or trough (see also Fig. 1). Of course, the homogeneous rough cases (1, 3, and 7) possess neither a crest nor a trough, but we have nonetheless recorded and presented data from towers located at the crest and trough locations of the spanwise heterogeneous cases. This presentation format is designed to maximize consistency between the presentation of results for the spanwise heterogeneous cases—for which spanwise averaging is not permitted—and the homogeneous cases. Moreover, it provides an additional sampling of data for the homogeneous cases, which thus helps to further justify the results.

A. Flow visualization

To illustrate the effect of spanwise-topographic heterogeneity on the inclination of coherent structures, we present instantaneous visualization of streamwise velocity fluctuations in the x - z plane. Figures 2(a)–2(c) and Figs. 2(d) and 2(e) correspond to planes above the crest and the trough, respectively, for case 1 [Figs. 2(a) and 2(d)], case 2 [Figs. 2(b) and 2(e)], and case 3 [Figs. 2(c) and 2(e)]. The instantaneous flow field is composed of alternating parcels of momentum excess (red) and deficit (blue), where the interfacial zones between such parcels exhibit consistent inclination. The vector map provides further information on vortical activity in the interfacial regions. This is entirely consistent with the spatially inclined nature of large-scale motions [17,27,58]. The “standard” inclination angle, $\theta \approx 15^\circ$, has not been annotated on the sketches, since the parcels of fluid are meandering spatially. In Sec. III C, results of a detailed computation of the inclination angle are shown. It will be shown that about the crest, the structures are relatively steeper due to enhanced mixing within high-momentum pathways; above the trough, the structures are unaffected by the secondary flows.

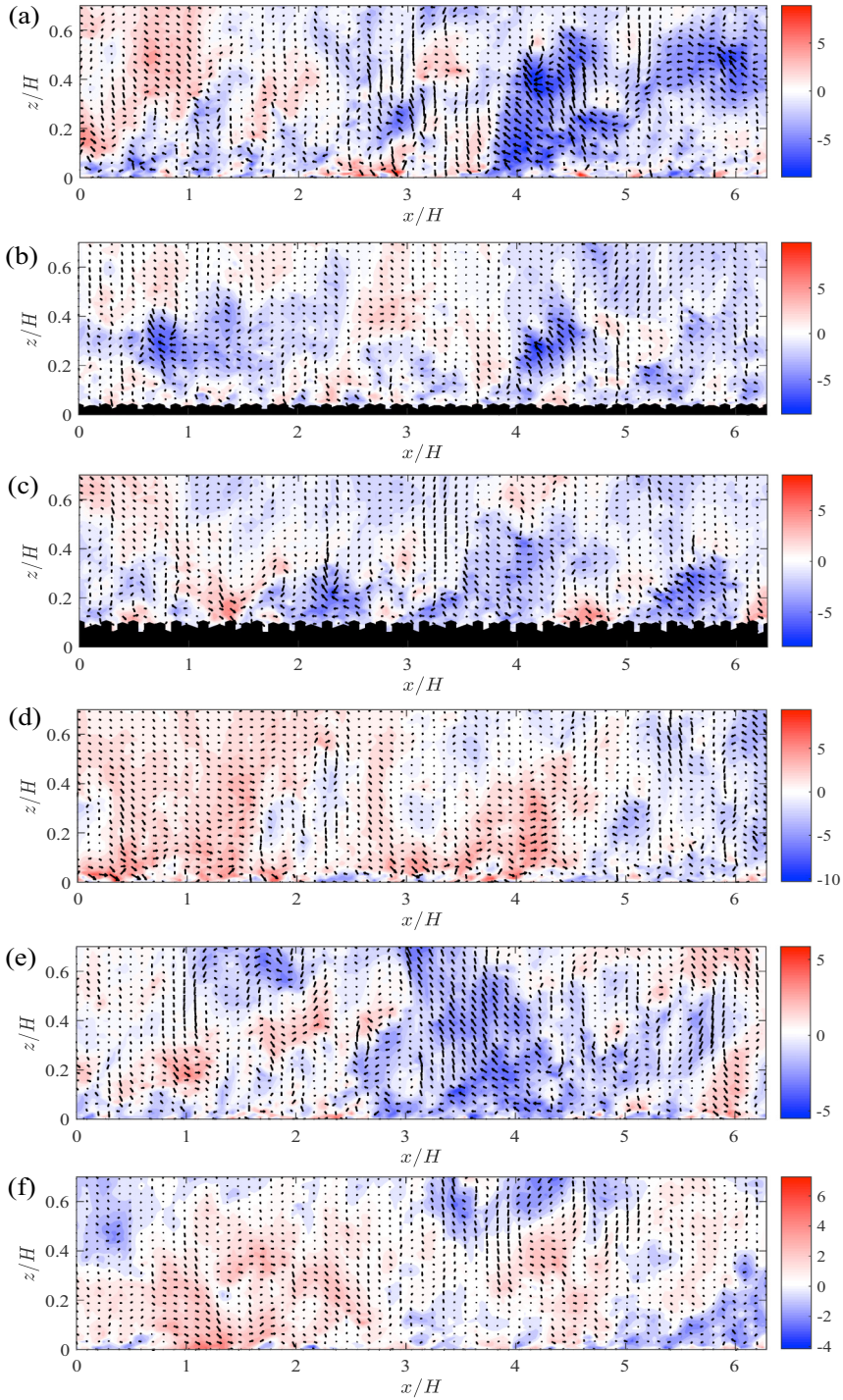


FIG. 2. Color flood contour of instantaneous streamwise velocity fluctuations, $\tilde{u}'(x, y_l, z, t_l)$, in the x - z plane at discrete spanwise location, y_l , at arbitrarily selected local time, t_l : (a)–(c) crest and (d)–(f) trough (see also Fig. 1). Vectors of $\{\tilde{u}'(x, y_l, z, t_l), \tilde{w}'(x, y_l, z, t_l)\}$ have been superimposed, for reference. (a), (d) Case 1, (b), (e) case 2, and (c), (f) case 3 (see also Table I).

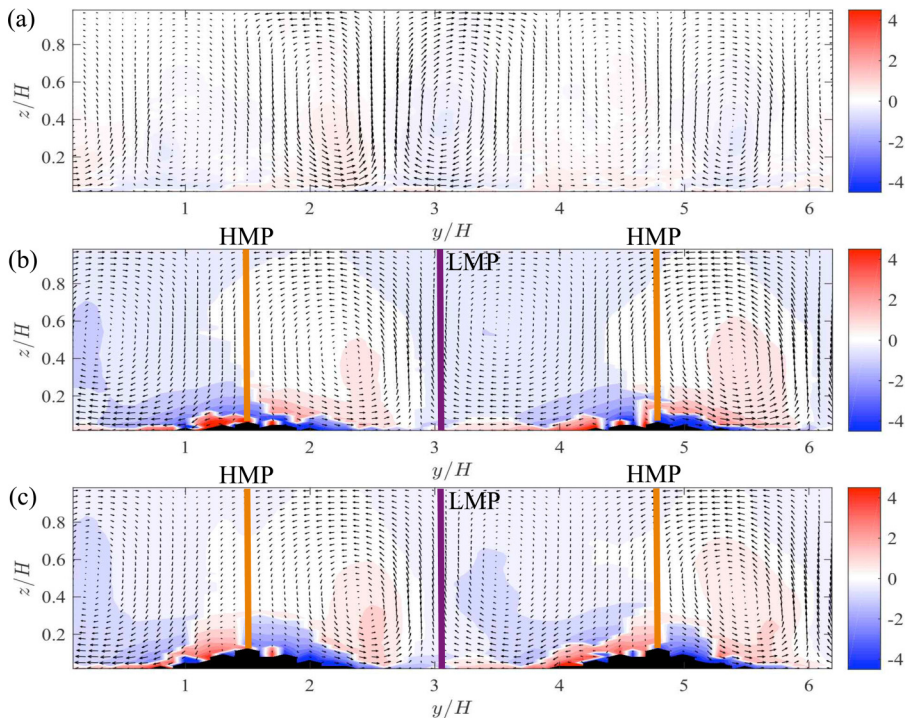


FIG. 3. Color flood contour visualization of time- and x -averaged swirl strength, $\langle \lambda_{ci} \rangle_{x,T}(y,z) \langle \tilde{\omega}_x \rangle_{x,T}(y,z) / \langle \tilde{\omega} \rangle_{x,T}(y,z)$, in the y - z plane, with $\{ \langle \tilde{v} \rangle_{x,T}(y,z), \langle \tilde{w} \rangle_{x,T}(y,z) \}$ vectors superimposed. (a) Case 1, (b) case 2, and (c) case 3 (see also Table I). In (b) and (c), we have added annotation for the location of topographically driven LMPs and HMPs.

As shown in the following figure, the crest is the “high-roughness” location, and we thus anticipate that the HMP should be located above this location [41–43]. It has been shown that the secondary flows are the product of a production-dissipation imbalance above the crest, where elevated turbulent kinetic energy (TKE) production above the crest necessitates a downwelling of low-TKE fluid from the outer region [51]. We contend, then, that the steepened structures are a manifestation of vigorous mixing above the crest, which attenuates large-scale correlation. Note, too, that structural steepening has been reported in other studies of flows over very rough walls [78,79]. In a subsequent section, we show that the qualitative observations of steepened structures in Figs. 2(a)–2(c) can be recorded in spatial correlations of fluctuating streamwise velocity.

Figures 2(d)–2(f) show quantities identical to those in Figs. 2(a)–2(c), but at a spanwise location corresponding with the domain trough (the homogeneous roughness cases—Figs. 2(a) and 2(d)—do not have a “crest” and “trough,” but we have nonetheless presented transects at the same locations to promote consistency with the other cases). As per Sec. III C, the structural inclination angle with LMPs is essentially equivalent to the inclination angle for flow over homogeneous roughness. Thus, above the “low roughness” and within LMPs [41], where the flow exhibits a mild upwelling [41,42], coherent structures meander through the domain and their structural attributes resemble those anticipated in canonical shear-driven wall turbulence [7]. Note, too, that while Fig. 2 corresponds with cases 1–3 (Table I), the other cases are in qualitative agreement (for brevity, we have not presented visualization for these cases).

Figure 3 shows the time- and streamwise-averaged swirl strength, signed by the mean streamwise vorticity, $\langle \lambda_x \rangle_{x,T}(y,z) \hat{i}_{\tilde{\omega}_x}$ [80], where $\hat{i}_{\tilde{\omega}_x} = \langle \tilde{\omega}_x \rangle_{x,T}(y,z) / \langle \tilde{\omega} \rangle_{x,T}(y,z)$ is the streamwise component of the Reynolds-averaged vorticity unit vector. Figure 3(a) shows a visualization for case 1, which

is the homogeneous roughness case and a benchmark against the effect of spanwise heterogeneity [Figs. 3(b) and 3(c), for cases 2 and 3, respectively]. We deliberately set all the color bar limits in Fig. 3 equivalent in order to make comparisons. It is clear that even for the homogeneous rough case, there are persistent rolls in the flow, although the results have been averaged for $\approx 10^3$ large-eddy turnovers. The presence of persistent spanwise–wall-normal rolls is well known in wall turbulence [81,82], and these rolls would likely remain after even further averaging. Nonetheless, relative to the cases with spanwise heterogeneity, their magnitude is relatively mild. This figure reveals the existence of alternating low- and high-momentum pathways [12], due to spanwise topographic heterogeneity. In this study, we fix the spanwise spacing between the adjacent Gaussian mounds to be $s_y/H > 2$. Therefore, the secondary flows are observed in both the roughness sublayer and inertial layer [44], although we note recent experimental research suggesting a reversal of the flow patterns for smaller spacing [45,52]. The upwelling and downwelling motions are present within LMPs and HMPs, respectively, which is consistent with previous findings [44]. Another conclusion that can be made from Fig. 3 is that the strength of the secondary flow increases with topographic height. Previous studies have revealed that secondary flows have an affect on the dynamics of the mean flow [41–43], and in this study we speculate that these secondary flows also have an impact on the mean inclination angle of the coherent structures and thus on the existence of any modulation of small-scale amplitude and frequency.

B. Profiles

Figure 4 shows vertical profiles of time- and streamwise-averaged streamwise [Figs. 4(a)–4(d)] and wall-normal [Figs. 4(e) and 4(f)] velocity components above the crest [Figs. 4(a), 4(c), and 4(e)] and trough [Figs. 4(b), 4(d), and 4(f)]. For Figs. 4(a) and 4(b), $\langle \tilde{u} \rangle_{x,T}(y_l, z)$ is normalized with the outer streamwise velocity, $U_0 = \langle \tilde{u} \rangle_{x,y,t}(z/H = 1)$, while for Figs. 4(c)–4(f), shear velocity is used to normalize velocity. From these figures, we can observe that the streamwise velocity profile above the crest and trough for cases 2 and 3 differs significantly from the homogeneous rough case. Above the crest [Fig. 4(a)], the outer-normalized velocity exhibits a prominent deficit in the lowest 10% of the domain, while for $(z - h_{\max})/H \gtrsim 0.2$, there is a modest (but significant) momentum excess, relative to the homogeneous rough case. This is entirely consistent with the underlying physics responsible for sustenance of the secondary flows, wherein near-wall production of turbulence is strongest and the vertical gradient in $\langle \tilde{u} \rangle_{x,T}(y_l, z)$ is most dramatic. Note, also, that with h_{\max} increasing, $\langle \tilde{u} \rangle_{x,T}(y_l, z)$ monotonically decreases. Above the trough, $\langle \tilde{u} \rangle_{x,T}(y_l, z)/U_0$ features a momentum deficit relative to the homogeneous case, and this is the location corresponding with the LMP.

When the vertical profiles of $\langle \tilde{u} \rangle_{x,T}(y_l, z)$ are normalized by $u_\tau(y_l)$ [Figs. 4(c) and 4(d)], the differences become more pronounced. First, between the locations corresponding with the crest and trough, note that the profiles for case 1 exhibit negligible differences (this result is precisely as expected, and is helpful when drawing comparisons to the cases perturbed by spanwise topographic heterogeneity). Above the crest, the $\langle \tilde{u} \rangle_{x,T}(y_l, z)/u_\tau(y_l)$ does not comply at all with logarithmic scaling, nor should it given the antecedent contributions upon which production-dissipation imbalances [51] are attributed to sustenance of the secondary flows [43]. We also see, again, that the profiles are monotonically reducing in streamwise momentum with increasing topographic height. Interestingly, however, above the trough we observe logarithmic scaling for $\langle \tilde{u} \rangle_{x,T}(y_l, z)/u_\tau(y_l)$ (or, at least, one could argue that the flow is closely approaching logarithmic scaling). Recall that within the LMPs, the spatial attributes of coherent structures were shown to resemble those found in canonical shear-driven wall turbulence, which suggests that HMPs are responsible for far greater departure from logarithmic conditions than LMPs (although, of course, they both coexist as a product of the same phenomenon).

Vertical profiles for $\langle \tilde{w} \rangle_{x,T}(y_l, z)/u_\tau(y_l)$ above the crest and trough are shown in Figs. 4(e) and 4(f), respectively. First, again note that for the homogeneous rough wall (case 1), $\langle \tilde{w} \rangle_{x,T}(y_l, z)/u_\tau(y_l) \approx 0$ throughout the depth of the flow, and as the averaging time approached infinity, the simulations

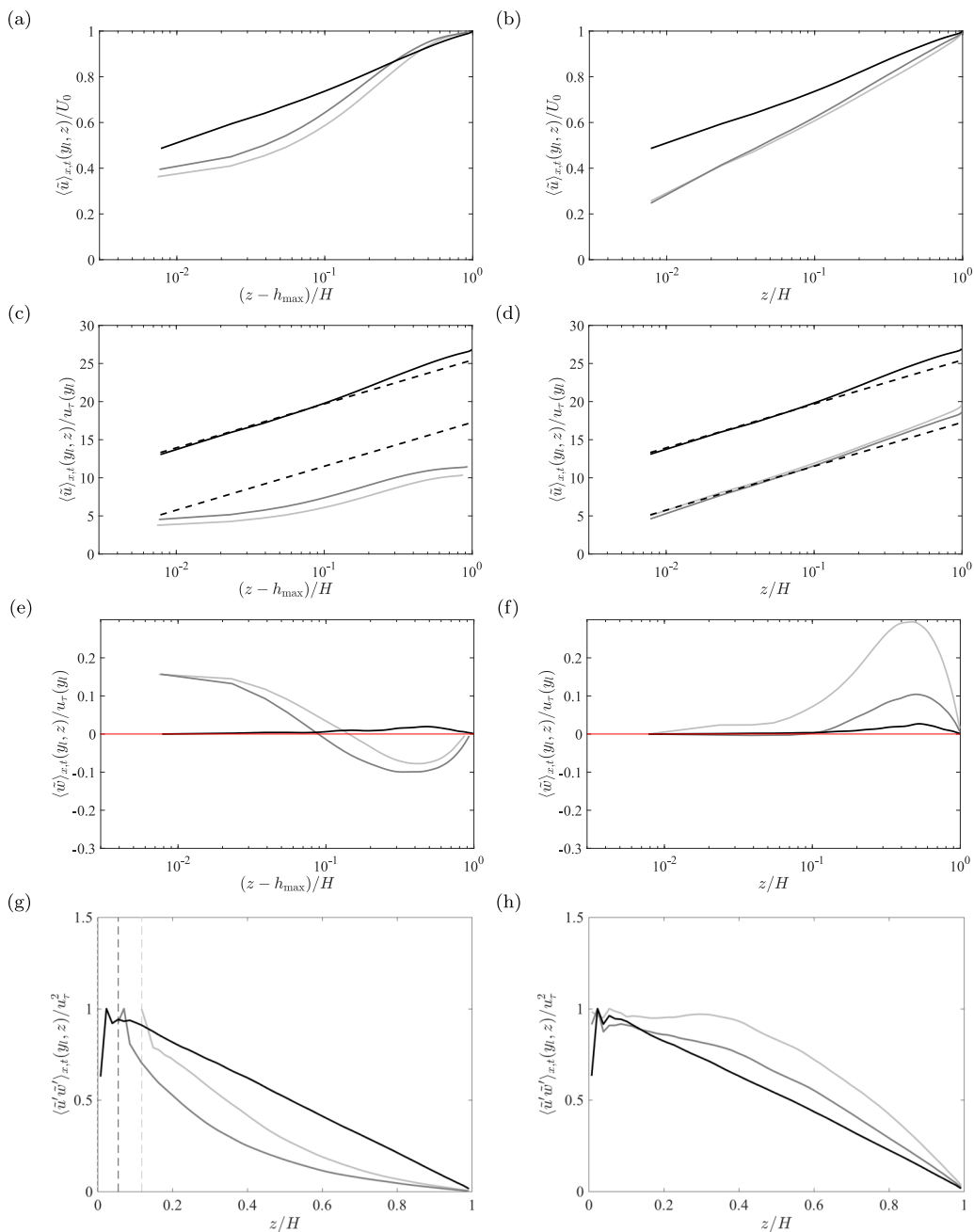


FIG. 4. Time- and streamwise-averaged vertical profiles of (a)–(f) first-order and (g), (h) second-order flow statistics. Profiles are derived from above the (a), (c), (e), (g) crest and (b), (d), (f), (h) trough, respectively. Profiles are normalized by (a), (b) the maximum advective velocity and (c)–(h) friction velocity, u_{τ} . Black, case 1; dark gray, case 2; and light gray, Case 3. Dashed black lines in (c), (d) denote the logarithmic profile with roughness length, z_0 , selected to optimally fit the LES data set. The horizontal dashed black lines in (g), (h) denote h_{\max}/H (see also Table I).

would predict $\langle \tilde{w} \rangle_{x,T}(y_l, z)/u_\tau(y_l) \rightarrow 0$. Above the crest, we see that $\langle \tilde{w} \rangle_{x,T}(y_l, z)/u_\tau(y_l)$ undergoes a change in sign at $z/H \approx 0.1$: for $z/H \lesssim 0.1$, $\langle \tilde{w} \rangle_{x,T}(y_l, z)/u_\tau(y_l) > 0$, while for $z/H \gtrsim 0.1$, $\langle \tilde{w} \rangle_{x,T}(y_l, z)/u_\tau(y_l) < 0$. The elevation over which $\langle \tilde{w} \rangle_{x,T}(y_l, z)/u_\tau(y_l) < 0$ approximately corresponds with the HMP discussed for Fig. 4(a), for $z/H \gtrsim 0.1$. The zone of downwelling is a product of local (roughness sublayer) circulations, which have been well documented in other studies [38,44,52]. Within the LMP [Fig. 4(f)], Reynolds-averaged upwelling is active over the depth of the flow, and the magnitude of upwelling increases for the more dramatic topography.

Figures 4(g) and 4(h) show vertical profiles of the Reynolds-averaged (total) streamwise–wall-normal momentum fluxes over the depth of the flow at the crest and trough, as outlined in the figure caption. Note that “total” here, with our wall-modeled LES [83], implies the sum of the resolved and subgrid-scale stresses, $\langle \mathbf{u}' \otimes \mathbf{u}' \rangle_T = \langle \tilde{\mathbf{u}}' \otimes \tilde{\mathbf{u}}' \rangle_T + \langle \boldsymbol{\tau} \rangle_T$. Note, first, that the momentum flux profiles are effectively equivalent for case 1 at the different locations, which serves as a basis for comparison with the cases perturbed by spanwise topographic heterogeneity. For cases 2 and 3, the Reynolds stress is redistributed due to spanwise heterogeneity, and a local friction velocity, $u_\tau(y_l) = (-\langle u'w' \rangle_{x,T}(y_l))^{1/2}$, must be introduced. For case 2 above the crest and trough, $u_\tau(y_l)/\langle u_\tau \rangle_y = 1.43$ and $u_\tau(y_l)/\langle u_\tau \rangle_y = 0.883$, respectively; for case 3 above the crest and trough, $u_\tau(y_l)/\langle u_\tau \rangle_y = 1.47$ and $u_\tau(y_l)/\langle u_\tau \rangle_y = 0.75$, respectively. This is consistent with enhanced momentum fluxes (i.e., drag) above the crest, due to elevated wall-normal gradients of streamwise velocity [Figs. 4(a) and 4(c)] and associated downwelling [Fig. 4(e)]. If we had normalized the vertical profiles of momentum fluxes by a spanwise-averaged shear velocity, $\langle u_\tau(y) \rangle_y$ (which is, by definition, unity in the present channel flow), we would immediately see that the stresses are larger in HMPs over the depth of the flow. Note that the profiles for the high-resolution cases (cases 4–9, Table I) compare favorably against the profiles shown for cases 1–3, and for brevity we have not included them here.

C. Structural attributes and topographic heterogeneity

The preceding sections have highlighted the dramatic extent to which topographically driven secondary flows alter turbulence characteristics relative to a canonical shear-driven channel. We have made numerous references to the steepening of coherent LSMs within the HMPs (Fig. 2 and accompanying Sec. III A text), and the implications of this for turbulence statistics (Fig. 4 and accompanying Sec. III B text). In order to fully clarify this result, and to provide confirmation of heretofore heuristic arguments, we have computed spatial cross correlations of the resolved fluctuating streamwise velocity at spanwise locations corresponding with the crest and trough:

$$\rho_{xx}(\delta x, y, z; z_{\text{Ref.}}) = \frac{\langle \tilde{u}'(x, y, z_{\text{Ref.}})u'(x + \delta x, y, z) \rangle_{xt}}{\sigma_x(z)^2}, \quad (14)$$

where δx is the streamwise separation, $z_{\text{Ref.}}$ is a wall-normal reference elevation, and σ_x is the root-mean-square value of the streamwise velocity fluctuation. In this article, we compute $\rho_{xx}(\delta x, y, z; z_{\text{Ref.}})$ during simulation and perform *a posteriori* time averaging, thereby eliminating the need to adopt Taylor’s frozen turbulence hypothesis and prescribe an advective velocity.

Figure 5 shows $\rho_{xx}(\delta x, y_l, z; z_{\text{Ref.}})$ color flood contours at spanwise locations, y_l , corresponding with the crest [Figs. 5(a), 5(c), and 5(e)] and trough [Figs. 5(b), 5(d), and 5(f)], respectively, for cases summarized in the caption. Black circles correspond with the maximum correlation,

$$\delta x_m(z; z_{\text{Ref.}}) = \underbrace{\text{argmax}}_{\delta x} [\rho_{xx}(\delta x, y_l, z; z_{\text{Ref.}})], \quad (15)$$

at each wall-normal location [26]. For the Fig. 5 correlations, we used $z_{\text{Ref.}}/H = 0.01$ at all spanwise locations corresponding with the trough [Figs. 5(b), 5(d), 5(f), and 5(h)]. For the correlation maps in Figs. 5(a), 5(c), and 5(e), we used $z_{\text{Ref.}}/H = 0.01$, $z_{\text{Ref.}}/H = 0.056$, and $z_{\text{Ref.}}/H = 0.12$, respectively, and these elevations have been superimposed on Fig. 5(g). These figures reveal that, as the topographic height is increased, the streamwise velocity correlation is diminished above the crest [Figs. 5(a), 5(c), and 5(e)], which was also reported by Yang and Anderson [44]. This

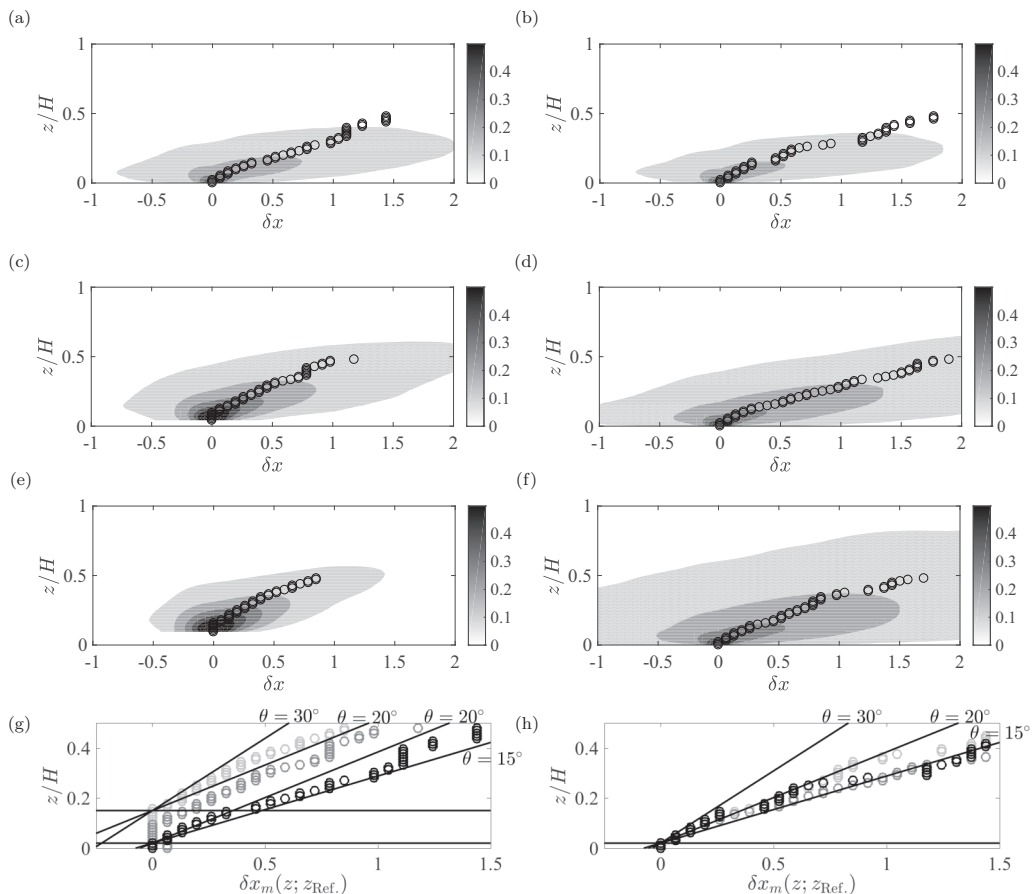


FIG. 5. Spatial correlation map of fluctuating streamwise velocity, $\rho_{xx}(\delta x, y, z; z_{\text{Ref.}})$ [Eq. (14)], in the streamwise lag-wall-normal plane for (a), (b), (d), (f) $z_{\text{Ref.}}/H = 0.01$, (c) $z_{\text{Ref.}}/H = 0.056$, and (e) $z_{\text{Ref.}}/H = 0.12$, above the (a), (c), (e) crest and (b), (d), (f) trough, respectively. Superimposed on the $\rho_{xx}(\delta x, y, z; z_{\text{Ref.}})$ color flood contours is the streamwise lag corresponding with maximum correlation, $\delta x_m(z; z_{\text{Ref.}})$ [Eq. (15)]. (a), (b) Case 1, (c), (d) case 2, and (e), (f) case 3. $\delta x_m(z; z_{\text{Ref.}})$ for cases 1–3 above the (g) crest and (h) trough, respectively, where solid horizontal lines denote the reference heights used in Eqs. (14) and (15), while the inclined solid lines are used to interpret the LES data points. Symbol colors correspond with case 1 (solid black), case 2 (solid dark gray), and case 3 (solid light gray).

result is consistent with prior findings on elevated mixing above the high-roughness regions, and the corresponding spatial decorrelation due to vigorous mixing. Above the trough, however, the correlation profiles are mostly similar, which is consistent with the results in Secs. III A and III B regarding the state of the flow within the present LMPs.

For all cases, we superimposed $\delta x_m(z; z_{\text{Ref.}})$ upon the correlation color floods in Figs. 5(a)–5(f). To complete the discussion, we summarized $\delta x_m(z; z_{\text{Ref.}})$ above the crest and trough in Figs. 5(g) and 5(h), respectively. To assist with interpretation of the LES data points, we added linear profiles at different inclinations, where $\theta = \tan^{-1}(\delta z/\delta x_m(z; z_{\text{Ref.}}))$ is the structural inclination angle.

As anticipated, above the trough [Fig. 5(h)], the data points all suggest a linear best fit with $\theta \approx 15^\circ$, which is entirely consistent with prior studies on flow over smooth or rough walls [16,17] (assuming validity of Townsend’s outer-layer similarity hypothesis [1]). Above the crest, however, the turbulence spatial attributes indicate a significant steepening. Thus, we contend that the established structural paradigm for rough wall flow structures encapsulated by hairpins remains valid, but the

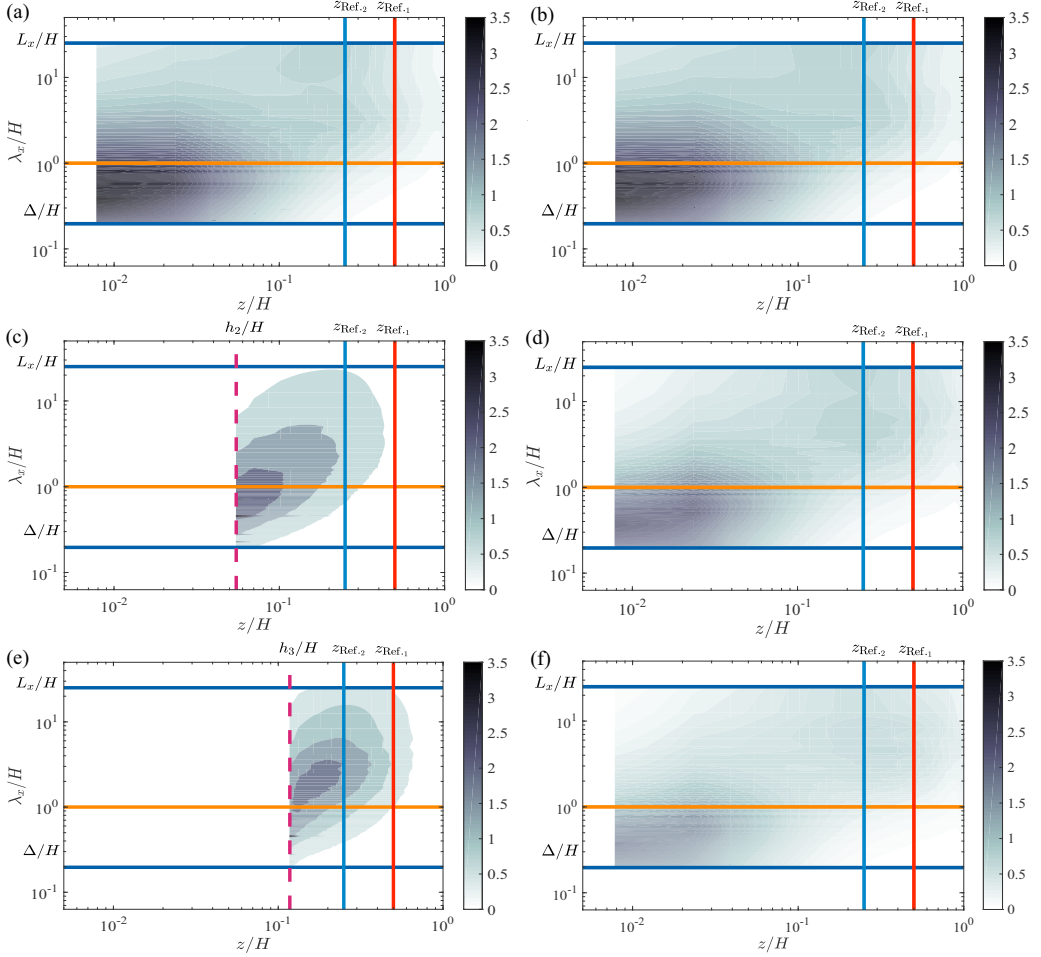


FIG. 6. Color flood contours of Fourier-mode spectrograms of \tilde{u}/u_τ . (a, b) Case 1, (c, d) case 2, and (e, f) case 3 above the (a, c, e) crest and (b, d, f) trough. Annotations have been added for the LES grid-filter width Δ/H , domain length L_x/H , and separation wavelength 2; we have also added annotations for two reference locations, $z_{\text{Ref},1}$ and $z_{\text{Ref},2}$, which are used in Sec. III E to determine two-point modulation of small-scale amplitude and frequency. For cases 2 and 3 above the crest, vertical dashed lines denote h_{max}/H .

hairpins themselves enclose steeper structures. This result is consistent with previous observations in this article, but its implications for modulation of small-scale amplitude and frequency have not received attention. In the following section, we demonstrate how topographically driven structural steepening shifts the outer peak to relatively shorter wavelengths, and how this affects the modulation correlation computations outlined in Sec. I B.

The correlation lengths summarized in Figs. 5(g) and 5(h) can be used to quantify the advective lag, $\lambda(z; z_{\text{Ref},i})$, required to compute two-point modulation correlations of small-scale amplitude and frequency [Eqs. (9) and (10)]. This was done *a posteriori* via the linear operation, $\lambda(z; z_{\text{Ref},i}) = \delta x_m(z; z_{\text{Ref},i})/U_0$, where for consistency with other aspects of this work we have set U_0 equivalent to the Reynolds-averaged channel centerline velocity.

D. Pre-multiplied energy spectra

Figure 6 shows contours of pre-multiplied energy spectra of resolved (LES) streamwise velocity, $k_x E_{\tilde{u}\tilde{u}'}/u_\tau^2$, where $k_x = 2\pi/\lambda_x$ is wave number and λ_x is wavelength [84]. These spectrograms

are based on projection on Fourier modes, as opposed to wavelets (discussion to follow). For the homogeneous rough case [Figs. 6(a) and 6(b)], we see a clear separation between the outer and inner peak, where the former is a product of VLSMs while the latter is a product of surface layer shear [84]. The separation wavelength, $\lambda_x/H = 2$, is used as a demarcation between the large and small scales, although as can be seen a range of values would ultimately yield the same outcome owing to the disparate length scales at which the outer and inner peaks reside [26,36,84]. Note also that the spectrograms at the two spanwise locations [Figs. 6(a) and 6(b)] are effectively equivalent, and both reveal the presence of a spectral plateau over the range $5 \lesssim \lambda_x/H \lesssim 10^1$. The case 1 spectrograms are not precisely equivalent, as they were taken from discrete virtual towers and we did not leverage spanwise homogeneity, as we would have otherwise done [26]; but the agreement is certainly reasonable and provides a foundation for assessing the role of topographically driven secondary flows.

Figures 6(c) and 6(d) and Figs. 6(e) and 6(f) show Fourier-based spectrograms for cases 2 and 3, respectively, at spanwise locations corresponding with the crest [Figs. 6(c) and 6(e)] and trough [Figs. 6(d) and 6(f)]. Considering first the crest, we see that the distinct outer peak has completely vanished, and spectral density diminishes with increasing wall-normal elevation and wavelength. There is, however, spectral density residing at wavelengths exceeding the large-scale cutoff noted in Sec. 1B, G_L , where $L = \delta_T U_0 H^{-1} = 2.0$, and results below demonstrate that this is sufficient for inducing a non-negligible modulation on the small scales across the depth of the flow. This argument is true for case 2 [Fig. 6(c)] and case 3 [Fig. 6(e)], although for case 3 the spectral density is vertically displaced by virtue of the topography. Note, too, that the series of elevated $k_x E_{\tilde{u}\tilde{u}'} / u_\tau^2$ above the topography, for both cases, is a product of vortex shedding from the roughness elements (Fig. 1).

For cases 2 and 3 above the trough [Figs. 6(d) and 6(f)], the spectrograms are ostensibly similar to that for the homogeneous roughness (case 1). However, closer inspection reveals an important difference: although the spectrograms indicate a distinct outer peak, it has shifted to smaller wavelengths ($\lambda_x/H \approx 8$), as opposed to the value $\lambda_x/H \approx 21$ expected for a pure channel. Moreover, by using color bars with equivalent quantitative range for all the spectrograms, it is apparent that variance (via Parseval’s theorem) is weaker in the “surface layer” region above the trough, all of which is consistent with antecedent results in this article and prior studies. Nonetheless, the spectrograms shown here indicate that large-scale motions in the present flows—even given the relatively extreme spanwise heterogeneity—should be capable of modulating the small scales. Since the correlations considered here [Eqs. (7)–(10)] are based on wavelet-based processing of the input time series (Sec. 1B), we have also prepared spectrograms of global wavelet power spectrum in frequency-height space.

Figure 7 shows wavelet-based spectrograms from virtual towers corresponding with the crest [Figs. 7(a), 7(c), and 7(e)] and trough [Figs. 7(b), 7(d), and 7(f)], for case 1 [Figs. 7(a) and 7(b)], case 2 [Figs. 7(c) and 7(d)], and case 3 [Figs. 7(e) and 7(f)]. Wavelet-based spectrograms are generated via the processing steps outlined in Sec. 1B, where the wavelet power spectrum, $E(z, t, f)$, is time averaged, yielding the global wavelet power spectrum, $G(z, f) = \langle E(z, t, f) \rangle_T$, which is then presented in the Fig. 7 color flood contours. Since $f \sim t^{-1}$, it follows that small frequency corresponds with large time (or length), and thus the wavelet-based spectrograms should approximately be a vertically mirrored version of the Fourier-based spectrograms; quick inspection of Fig. 7 proves this to be true. Although the spectrograms show undulations in the frequency-height space, which are due to insufficiently long time-averaging periods, salient features of the flow are nonetheless captured and the results are consistent with the Fourier-based projection (Fig. 6 and accompanying text).

Figures 7(a) and 7(b) show the accumulation of spectral density at high frequencies within the roughness sublayer ($z/H \lesssim 0.1$). Since these panels are for the homogeneous roughness case, such that the two spanwise locations are physically equivalent, no substantial differences can be expected between the panels (beyond, simply, the effects of averaging). Figures 7(a) and 7(b) show the selected separation frequency, f_c (orange line), which has clearly been placed within the band

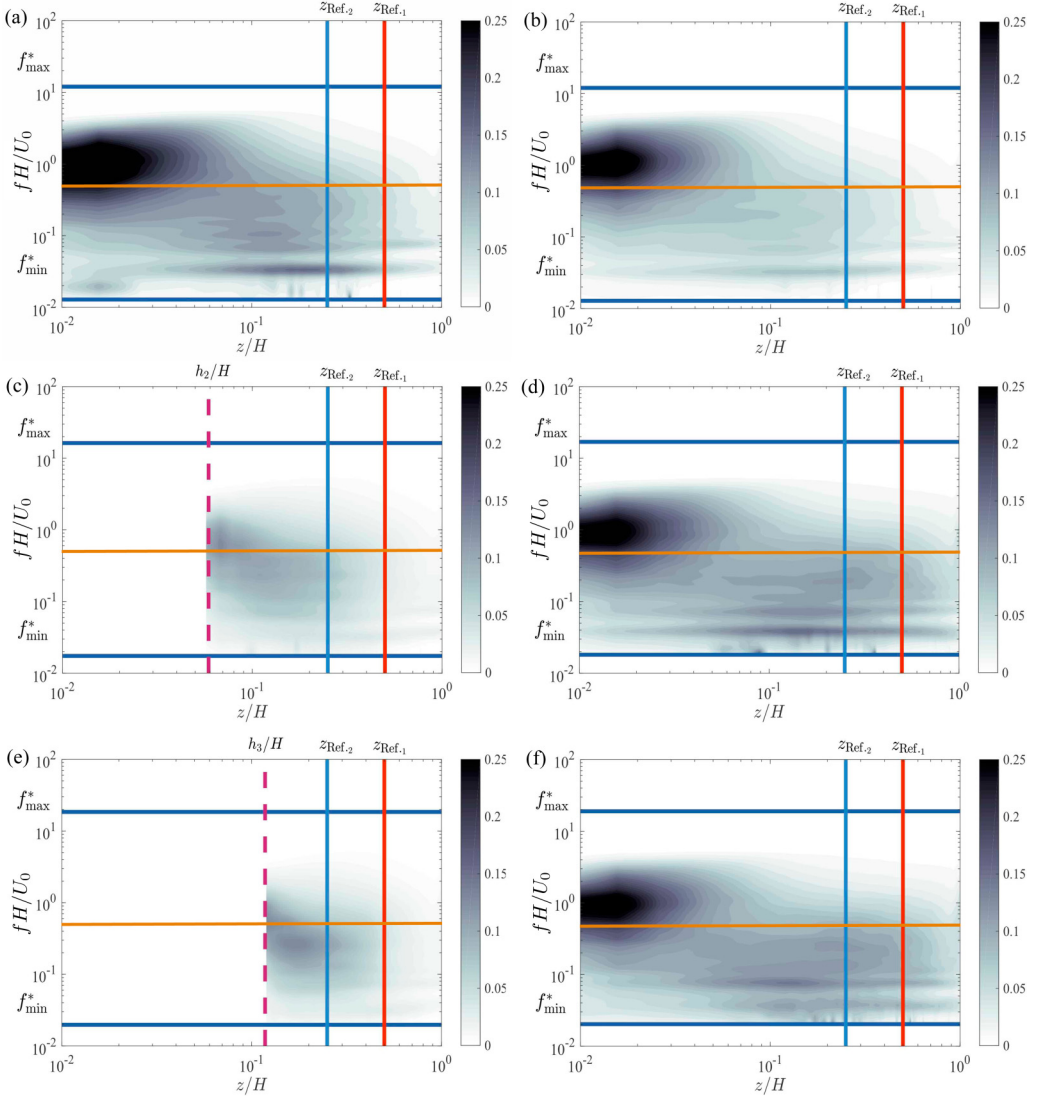


FIG. 7. Color flood contours of wavelet-based spectrograms of \tilde{u}/u_τ . (a), (b) Case 1, (c), (d) case 2, and (e), (f) case 3 above the (a), (c), (e) crest and (b), (d), (f) trough. Annotations have been added for the shear-normalized LES grid-filter frequency $f_{\min}^* H/U_0$, domain length $f_{\max}^* H/U_0$, and shear-normalized separation frequency $f_c H/U_0 = 0.5$; we have also added annotations for two reference locations, $z_{\text{Ref},1}$ and $z_{\text{Ref},2}$, which are used in Sec. III E to determine two-point modulation of small-scale amplitude and frequency. For cases 2 and 3 above the crest, vertical dashed lines denote h_{\max}/H .

of frequencies between the inner and outer peaks. In fact, since the inner and outer peaks reside at different frequencies, we could have used a large range of frequencies to separate the large and small scales. In work not presented here, we experimented with different f_c and found no discernible influence on the statistics, which is consistent with the complementary work of Ganapathisubramani *et al.* [33].

For cases 2 and 3, the wavelet-based spectrograms above the trough are, at first glance, spatially similar to that for case 1 [Figs. 7(d) and 7(f)]. However, closer inspection reveals that the outer peak, which was located at $fH/U_0 \approx 0.03$ for case 1 [Figs. 7(a) and 7(b)], has shifted to higher frequencies

($fH/U_0 \approx 0.07$), which is consistent with observations of the Fourier-based spectrograms. This result, by itself, demonstrates that while flow processes within LMPs may appear unaffected by the secondary motions to first order [i.e., Figs. 2(e) and 2(f) or Figs. 4(b) and 4(d)], higher-order statistics reveal nontrivial modifications.

Figures 7(c) and 7(e) show wavelet-based spectrograms above the crest for cases 2 and 3, where the separation frequency, f_c , and maximum topographic height have been annotated for discussion. As per Fig. 6, there are no longer two distinct peaks residing at different wavelengths (or frequencies), and instead spectral density is clustered around f_c . At frequencies exceeding f_c , this result is consistent with the presence of vigorous roughness sublayer mixing above the topography, while for frequencies less than f_c , the result indicates that the outer peak has vanished. This demonstrates that downwelling and the associated vigorous mixing within HMPs attenuates large-scale correlation, and only relatively smaller structures are preserved. We nonetheless show that sub- f_c structures are capable of imposing a modulation of the small-scale frequency and amplitude.

E. Correlation profiles

Figures 8 and 9 show the single- and two-point correlation profiles for modulation of small-scale amplitude and frequency, respectively, as per the postprocessing procedure outlined in Sec. 1B [34,35]. Equations (7)–(10) quantify how the large-scale content, $\tilde{u}'_L(x_l, y_l, z, t)$, correlates with the amplitude and frequency embodied in the small scales. Though more cumbersome, consideration of two-point correlations (right ordinates of Figs. 8 and 9) provides the best context for assessing how the passage of structures in the outer layer is correlated with the dynamics of the near-wall region.

In the interest of brevity, we opted to show only correlations for cases 1 and 3, these being the limiting cases considered (all prior statistics in this paper have reported monotonic trends, and we can report similar properties for the amplitude and frequency modulation profiles of the intermediate cases). We have, however, shown the profiles across resolutions (in Figs. 8 and 9, black, dark gray, and light gray correspond with low-, intermediate-, and high-resolution versions of the same flow-topography arrangement, respectively). Establishing insensitivity to computational mesh resolution is of pivotal importance to studies of amplitude and frequency modulation [36], since such insensitivity demonstrates that the conceptual framework of any predictive model [28] can be utilized in a general sense. We made our best efforts to integrate the high-resolution cases for a sufficiently long time [77], although these cases do present logistical challenges. For this reason, statistics for the high-resolution cases (cases 7–9; Table I) were based on averaging over a period, $TU_0H^{-1} \approx 10^3$, approximately 30% and 20% of the averaging period used for the intermediate (cases 4–6) and low resolution (cases 1–3), respectively. Thus, we observe generally strong agreement between the low- and intermediate-resolution cases, both of which deviate modestly from the high-resolution cases. These results add to evidence that existing techniques for quantifying amplitude and frequency modulation [34] are not susceptible to mesh resolution [36]. This result is compliant with the conceptual foundations of LES, wherein Reynolds-averaged turbulence quantities should be equivalent even as the subgrid- and resolved-scale contributions vary with varying filter scale.

Beginning first with the vertical profiles for amplitude modulation (Fig. 8), it is apparent that the single- and two-point correlations for all cases are correctly equivalent at the reference heights. We also see that the amplitude modulation profiles are very similar above the “crest” and “trough” for cases 1, 4, and 7 [Figs. 8(a), 8(b), 8(e), and 8(f)], which is a logical consequence of the spatially homogeneous surface conditions for these cases. Moreover, we see that $|R_a(z; z)| \gtrsim |R_a(z; z_{\text{Ref}})|$ over the depth of the flow, since the small scales are closely correlated with large scales at the same height. However, for $z_{\text{Ref},1}/H = 0.5$, there is a narrow range, $0.1 \lesssim z/H \lesssim 0.2$, where $|R_a(z; z)| < |R_a(z; z_{\text{Ref}})|$; the Fourier- and wavelet-based spectrograms (Figs. 6 and 7, respectively) indicate that $z_{\text{Ref},1}/H$ is “above” the outer peak, while the range in which $|R_a(z; z)| < |R_a(z; z_{\text{Ref}})|$ corresponds with the spectral plateau. Since the input argument, $\sigma'_{SL}(z, t)$, does not change between Eqs. (7) and (9), the differences must be generated by differences to the large scale, $\tilde{u}'_L(z_{\text{Ref}}, \tau(z; z_{\text{Ref}}))$: the zone of $|R_a(z; z)| < |R_a(z; z_{\text{Ref}})|$ is thus attributed to the persistent momentum excess above the crest,

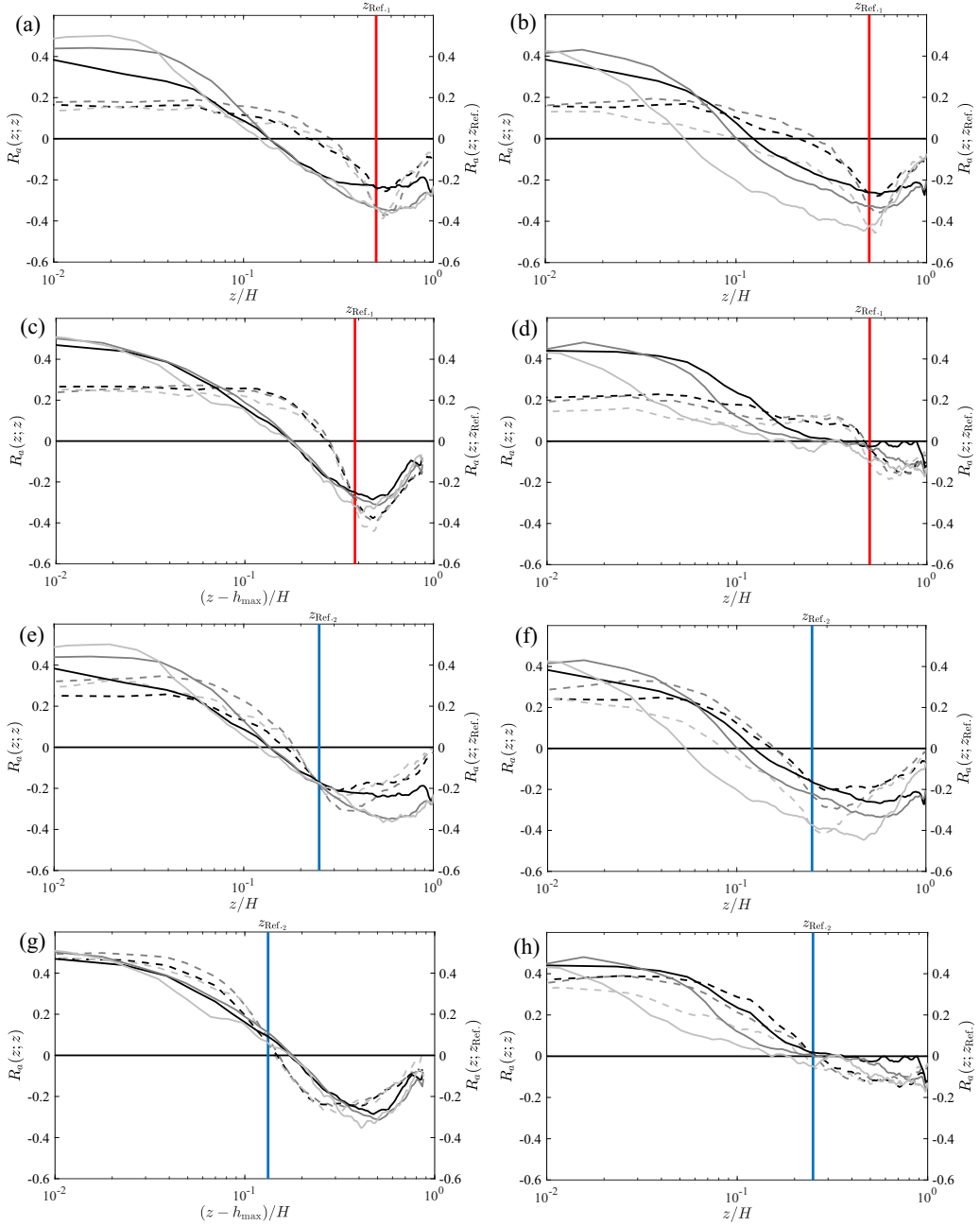


FIG. 8. Vertical profiles for small-scale amplitude modulation by large scale, $\tilde{u}'_L(x_l, y_l, z, t)$, at discrete streamwise-spanwise locations, $\{x_l, y_l\}$, corresponding with the (a), (c), (e), (g) crest and (b), (d), (f), (h) trough. Dashed and solid profiles correspond with single-point [Eq. (7)] and two-point [Eq. (9)] correlation, respectively, and corresponding values for both are shown by the left and right figure ordinates. (a), (b), (e), (f) Black, dark gray, and light gray correspond with cases 1, 4, and 7, respectively; (c), (d), (g), (h) black, dark gray, and light gray correspond with cases 3, 6, and 9, respectively. The reference heights used for (a)–(d) and (e)–(h) are $z_{\text{Ref},1}/H = 0.5$ (red) and $z_{\text{Ref},2}/H = 0.25$ (blue), respectively, and both were included on the spectrograms (Figs. 6 and 7).

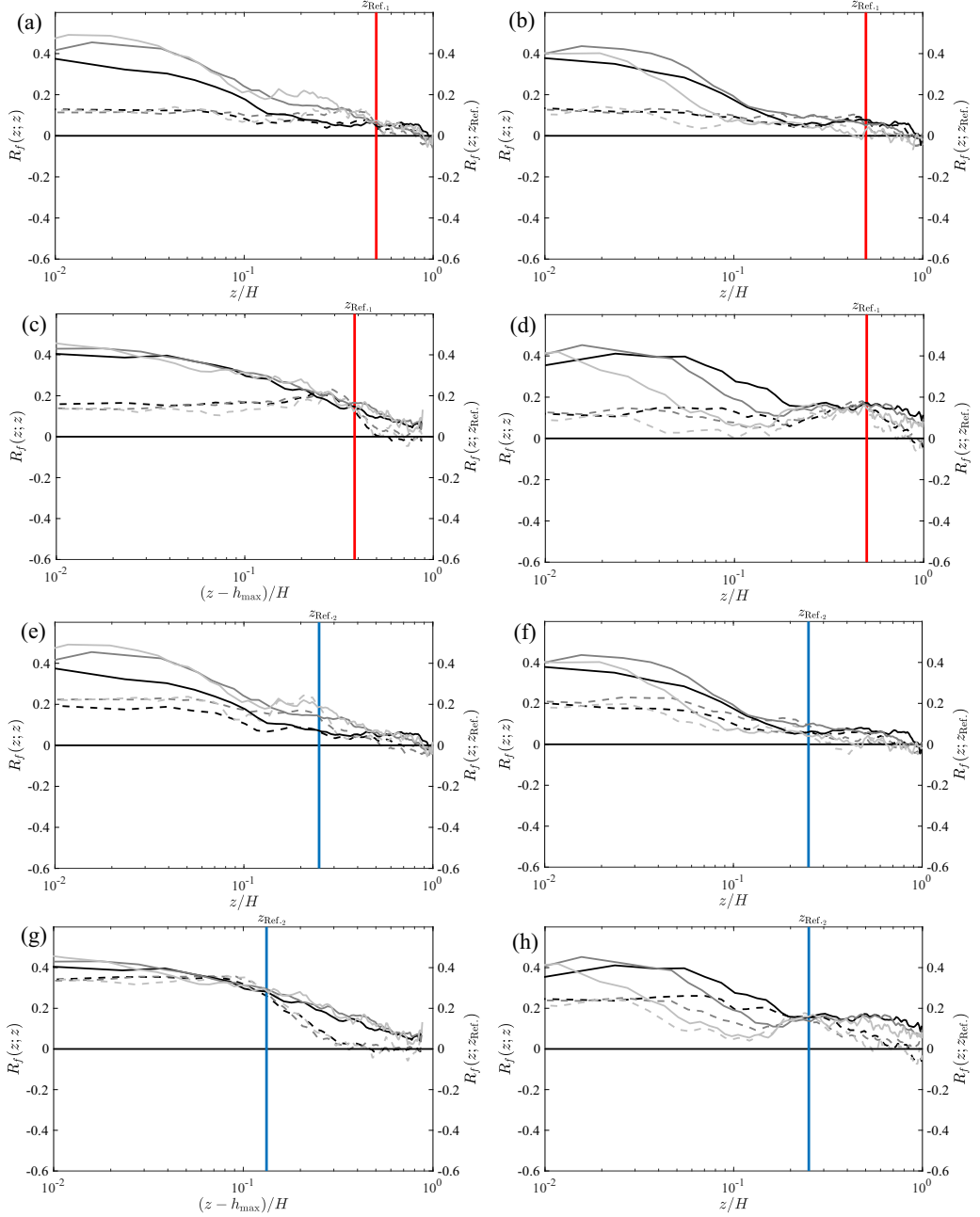


FIG. 9. Vertical profiles for small-scale frequency modulation by large scale, $\tilde{u}'_L(x_l, y_l, z, t)$, at discrete streamwise-spanwise locations, $\{x_l, y_l\}$, corresponding with the (a), (c), (e), (g) crest and (b), (d), (f), (h) trough. Dashed and solid profiles correspond with single-point [Eq. (8)] and two-point [Eq. (10)] correlation, respectively, and corresponding values for both are shown by the left and right figure ordinates. (a), (b), (e), (f) Black, dark gray, and light gray correspond with cases 1, 4, and 7, respectively; (c), (d), (g), (h) black, dark gray, and light gray correspond with cases 3, 6, and 9, respectively. The reference heights used for (a)–(d) and (e)–(h) are $z_{\text{Ref},1}/H = 0.5$ (red) and $z_{\text{Ref},2}/H = 0.25$ (blue), respectively, and both were included on the spectrograms (Figs. 6 and 7).

associated with the HMP. Note, too, that the correlations cross over at $z/H \approx 0.1$, below which $|R_a(z; z)| > |R_a(z; z_{\text{Ref.}})|$.

Interestingly, for $z_{\text{Ref.1}}/H$, amplitude modulation above the trough [Figs. 8(b) and 8(d)] shows much closer agreement between cases 1, 4, and 7 relative to cases 3, 6, and 9. We have argued and demonstrated in all preceding stages of this article that—at least for the topographies considered—it is within HMPs (above crest) that flow physics are most dramatically perturbed, while LMPs (above the trough) are far less disruptive to the structural characteristics expected for canonical shear-driven channel flow turbulence. Figures 8(b) and 8(d) and Figs. 8(f) and 8(h) provide further support for this conclusion.

From Figs. 6 and 7, it is clear that $z_{\text{Ref.1}}/H$ does not intersect the outer peak, and for this reason we considered the second location, $z_{\text{Ref.2}}/H$, which strikes precisely through the outer peak for the homogeneous rough case and above the trough for the spanwise-heterogeneous cases. We subsequently observe a much closer agreement between the single- and two-point correlations [35]. For cases 3, 6, and 9, despite the lack of any distinct outer peak [Figs. 6(e) and 7(e)], we nonetheless find strong correlations. Above the crest, elevated production of turbulence ultimately attenuates large-scale correlation in the flow, and instead spectral density is concentrated in a larger zone. However, the underlying approach to amplitude modulation, which is predicated upon Parseval's theorem, is contingent only upon the variance within the flow, not the wavelength or frequency at which spectral density resides.

Figure 9 shows the frequency modulation correlations for cases 1, 4, and 7 [Figs. 9(a), 9(b), 9(e), and 9(f)] and cases 3, 6, and 9 [Figs. 9(c), 9(d), 9(g), and 9(h)], above the crest [Figs. 9(a), 9(c), 9(e), and 9(g)] and trough [Figs. 9(b), 9(d), 9(f), and 9(h)], for reference elevations, $z_{\text{Ref.1}}/H$ [Figs. 9(a)–9(d)] and $z_{\text{Ref.2}}/H$ [Figs. 9(e)–9(h)], cited in the figure caption. As per Fig. 8, there is some disagreement between the high-resolution cases and those for the intermediate- and low-resolution cases, although the overall trends agree. For these cases, $R_f(z; z) > R_f(z; z_{\text{Ref.}})$, with the exception of $z = z_{\text{Ref.}}$, at which elevation the correlations are by definition equivalent. The single-point correlation continues to rise as the surface is approached, while the two-point correlations (above the crest and trough) remain constant with depth after reaching their upper limit. Moreover, we again see that when the reference elevation is selected to intersect the outer peak, the single- and two-point correlations agree closely over a large vertical region, relative to when the reference location does not intersect the outer peak. Note, too, that the frequency modulation profiles above the trough for cases 1, 4, and 7 are similar to those above the trough for cases 3, 6, and 9, which is consistent with all previous findings regarding the modestly disruptive influence of LMPs, relative to HMPs.

IV. CONCLUSION

We used LES to systematically explore how topographically driven turbulent secondary flows disrupt the spatial nature of turbulent flow physics in a channel, and presented all results against a benchmark homogeneous roughness. The spanwise-heterogeneous topographies were constructed with element-to-element multiplication of two-dimensional Gaussian distributions, which yields topographies with a prominent spanwise heterogeneity that are also undulating in the streamwise direction. For the inertial-dominated, fully rough flow conditions considered in this study, the results (and scientific conclusions) are expected to transcend topographic arrangements; that is, provided the lower surface is capable of sustaining domain-scale secondary flows in the form of HMPs and LMPs, results for different surfaces should closely resemble those presented here. We recognize that in recent times this topic has received attention, and the role of spacing between spanwise-adjacent heterogeneities has been under consideration [44,45,52], but for the very large spanwise spacing considered here we expect the HMPs and LMPs to be clearly anchored above the crest and trough, respectively [41,43].

We have systematically demonstrated that within HMPs, large-scale correlation is attenuated by virtue of vigorous mixing above the crest, and VLSMs are absent. Within LMPs, however, large-scale

correlation in the form of VLSPs is mostly preserved, although the signature of their presence shifts to shorter wavelengths. This is shown qualitatively and via assessment of first- and second-order turbulence statistics. This is somewhat surprising, since LMPs and HMPs coexist as a product of the same external condition—spanwise topographic heterogeneity—and yet LMPs appear far less influential to the flow physics.

These results were viewed in the context of small-scale frequency and amplitude modulation by the large scales. We showed that frequency and amplitude modulation profiles are relatively similar within HMPs and LMPs, relative to the benchmark homogeneous rough case. We also showed that the presently used measure of small-scale amplitude and frequency modulation is sensitive to the choice of outer, reference elevation. When the reference elevation intercepts the outer peak, the single- and two-point correlations are similar over a larger range of elevations, relative to when the reference height does not intersect the outer peak. We modeled flow over the three topographies with three different resolutions, which provided an opportunity to assess any sensitivity to resolution. We found virtually no dependence on resolution, which bodes well for longer-term efforts to incorporate these concepts into development of surface flux closures for deployment in wall-modeled LES.

ACKNOWLEDGMENTS

This work was supported by the Air Force Office of Scientific Research under Grants No. FA9550-14-1-0101 and No. FA9550-14-1-0394. Computational resources were provided by the Texas Advanced Computing Center at the University of Texas and the Office of Information Technology at the University of Texas at Dallas.

-
- [1] A. A. Townsend, *The Structure of Turbulent Shear Flow* (Cambridge University Press, Cambridge, UK, 1976).
 - [2] S. J. Kline, W. C. Reynolds, F. A. Schraub, and P. W. Runstadler, The structure of turbulent boundary layers, *J. Fluid Mech.* **30**, 741 (1967).
 - [3] K. N. Rao, R. Narasimha, and M. A. Badri Narayanan, The bursting phenomena in a turbulent boundary layer, *J. Fluid Mech.* **48**, 339 (1971).
 - [4] P. R. Bandyopadhyay and A. K. M. F. Hussain, The coupling between scales in shear flows, *Phys. Fluids* **27**, 2221 (1984).
 - [5] W. Schoppa and F. Hussain, Coherent structure generation in near-wall turbulence, *J. Fluid Mech.* **453**, 57 (2002).
 - [6] C. D. Meinhart and R. J. Adrian, On the existence of uniform momentum zones in a turbulent boundary layer, *Phys. Fluids* **7**, 694 (1995).
 - [7] N. Hutchins and I. Marusic, Evidence of very long meandering features in the logarithmic region of turbulent boundary layers, *J. Fluid Mech.* **579**, 1 (2007).
 - [8] R. J. Adrian, C. D. Meinhart, and C. D. Tomkins, Vortex organization in the outer region of the turbulent boundary layer, *J. Fluid Mech.* **422**, 1 (2000).
 - [9] R. J. Adrian, Hairpin vortex organization in wall turbulence, *Phys. Fluids* **19**, 041301 (2007).
 - [10] A. J. Grass, Structural features of turbulent flow over smooth and rough boundaries, *J. Fluid Mech.* **50**, 233 (1971).
 - [11] M. R. Raupach, R. A. Antonia, and S. Rajagopalan, Rough-wall turbulent boundary layers, *Appl. Mech. Rev.* **44**, 1 (1991).
 - [12] R. Mejia-Alvarez and K. T. Christensen, Low-order representations of irregular surface roughness and their impact on a turbulent boundary layer, *Phys. Fluids* **22**, 015106 (2010).
 - [13] J. Jimenez, Turbulent flow over rough wall, *Annu. Rev. Fluid Mech.* **36**, 173 (2004).
 - [14] I. P. Castro, Rough-wall boundary layers: Mean flow universality, *J. Fluid Mech.* **585**, 469 (2007).

- [15] B. Ganapathisubramani, E. K. Longmire, and I. Marusic, Characteristics of vortex packets in turbulent boundary layers, *J. Fluid Mech.* **478**, 35 (2003).
- [16] R. J. Volino, M. P. Schultz, and K. A. Flack, Turbulence structure in rough- and smooth-wall boundary layers, *J. Fluid Mech.* **592**, 263 (2007).
- [17] Y. Wu and K. T. Christensen, Outer-layer similarity in the presence of a practical rough-wall topology, *Phys. Fluids* **19**, 085108 (2007).
- [18] J. Hong, J. Katz, C. Meneveau, and M. Schultz, Coherent structures and associated subgrid-scale energy transfer in a rough-wall channel flow, *J. Fluid Mech.* **712**, 92 (2012).
- [19] K. C. Kim and R. J. Adrian, Very large-scale motion in the outer layer, *Phys. Fluids* **11**, 417 (1999).
- [20] B. J. Balakumar and R. J. Adrian, Large- and very-large-scale motions in channel and boundary-layer flows, *Philos. Trans. R. Soc. A* **365**, 665 (2007).
- [21] D. J. C. Dennis and T. B. Nickels, Experimental measurement of large-scale three-dimensional structures in a turbulent boundary layer. Part 1. Vortex packets, *J. Fluid Mech.* **673**, 180 (2011).
- [22] D. J. C. Dennis and T. B. Nickels, Experimental measurement of large-scale three-dimensional structures in a turbulent boundary layer. Part 2. Long structures, *J. Fluid Mech.* **673**, 218 (2011).
- [23] J. Ahn, J. H. Lee, J. Lee, J.-H. Kang, and H. J. Sung, Direct numerical simulation of a 30R long turbulent pipe flow at $Re_\tau = 3008$, *Phys. Fluids* **27**, 065110 (2015).
- [24] L. H. O. Hellström, B. Ganapathisubramania, and A. J. Smits, The evolution of large-scale motions in turbulent pipe flow, *J. Fluid Mech.* **779**, 701 (2015).
- [25] J. Fang and F. Porté-Agel, Large-eddy simulation of very-large-scale motions in the neutrally stratified atmospheric boundary layer, *Boundary-Layer Meteorol.* **155**, 397 (2015).
- [26] C. Jacob and W. Anderson, Conditionally averaged large-scale motions in the neutral atmospheric boundary layer: Insights for aeolian processes, *Boundary-Layer Meteorol.* **162**, 21 (2017).
- [27] Y. Wu and K. T. Christensen, Spatial structure of a turbulent boundary layer with irregular surface roughness, *J. Fluid Mech.* **655**, 380 (2010).
- [28] I. Marusic, R. Mathis, and N. Hutchins, Predictive model for wall-bounded turbulent flow, *Science* **329**, 193 (2010).
- [29] R. Mathis, N. Hutchins, and I. Marusic, Large-scale amplitude modulation of the small-scale structures in turbulent boundary layers, *J. Fluid Mech.* **628**, 311 (2009).
- [30] R. Mathis, N. Hutchins, and I. Marusic, A predictive inner-outer model for streamwise turbulence statistics in wall-bounded flows, *J. Fluid Mech.* **681**, 537 (2011).
- [31] R. Mathis, I. Marusic, S. I. Chernyshenko, and N. Hutchins, Estimating wall-shear-stress fluctuations given an outer region input, *J. Fluid Mech.* **715**, 163 (2013).
- [32] K. M. Talluru, R. Baidya, N. Hutchins, and I. Marusic, Amplitude modulation of all three velocity components in turbulent boundary layers, *J. Fluid Mech.* **746**, R1 (2014).
- [33] B. Ganapathisubramani, N. Hutchins, J. P. Monty, D. Chung, and I. Marusic, Amplitude and frequency modulation in wall turbulence, *J. Fluid Mech.* **712**, 61 (2012).
- [34] W. J. Baars, M. K. Talluru, N. Hutchins, and I. Marusic, Wavelet analysis of wall turbulence to study large-scale modulation of small scales, *Exp. Fluids* **56**, 188 (2015).
- [35] G. Pathikonda and K. T. Christensen, Inner-outer interactions in a turbulent boundary layer overlying complex roughness, *Phys. Rev. Fluids* **2**, 044603 (2017).
- [36] W. Anderson, Amplitude modulation of streamwise velocity fluctuations in the roughness sublayer: Evidence from large-eddy simulations, *J. Fluid Mech.* **789**, 567 (2016).
- [37] D. T. Squire, W. J. Baars, N. Hutchins, and I. Marusic, Inner-outer interactions in rough-wall turbulence, *J. Turbul.* **17**, 1159 (2016).
- [38] D. B. Goldstein and T.-C. Tuan, Secondary flow induced by riblets, *J. Fluid Mech.* **363**, 115 (1998).
- [39] R. Mejia-Alvarez and K. T. Christensen, Wall-parallel stereo particle-image velocimetry measurements in the roughness sublayer of turbulent flow overlying highly irregular roughness, *Phys. Fluids* **25**, 115109 (2013).
- [40] B. Nugroho, N. Hutchins, and J. P. Monty, Large-scale spanwise periodicity in a turbulent boundary layer induced by highly ordered and directional surface roughness, *Int. J. Heat Fluid Flow* **41**, 90 (2013).

- [41] D. Willingham, W. Anderson, K. T. Christensen, and J. Barros, Turbulent boundary layer flow over transverse aerodynamic roughness transitions: Induced mixing and flow characterization, *Phys. Fluids* **26**, 025111 (2013).
- [42] J. M. Barros and K. T. Christensen, Observations of turbulent secondary flows in a rough-wall boundary layer, *J. Fluid Mech.* **748**, R1 (2014).
- [43] W. Anderson, J. M. Barros, K. T. Christensen, and A. Awasthi, Numerical and experimental study of mechanisms responsible for turbulent secondary flows in boundary layer flows over spanwise heterogeneous roughness, *J. Fluid Mech.* **768**, 316 (2015).
- [44] J. Yang and W. Anderson, Numerical study of turbulent channel flow over surfaces with variable spanwise heterogeneities: Topographically-driven secondary flows affect outer-layer similarity of turbulent length scales, *Flow, Turbul. Combust.* **100**, 1 (2017).
- [45] T. Medjnoun, C. Vanderwel, and B. Ganapathisubramani, Characteristics of turbulent boundary layers over smooth surfaces with spanwise heterogeneities, *J. Fluid Mech.* **838**, 516 (2018).
- [46] H. G. Hwang and J. H. Lee, Secondary flows in turbulent boundary layers over longitudinal surface roughness, *Phys. Rev. Fluids* **3**, 014608 (2018).
- [47] P. Bradshaw, Turbulent secondary flows, *Annu. Rev. Fluid Mech.* **19**, 53 (1987).
- [48] L. Prandtl, *Essentials of Fluid Dynamics* (Springer, New York, NY, 1952).
- [49] J. Nikuradse, Laws of flow in rough pipes, NACA Technical Memorandum 1292, 1933 (unpublished).
- [50] E. Brundrett and W. D. Baines, The production and diffusion of vorticity in duct flow, *J. Fluid Mech.* **19**, 375 (1964).
- [51] J. O. Hinze, Secondary currents in wall turbulence, *Phys. Fluids* **10**, S122 (1967).
- [52] C. Vanderwel and B. Ganapathisubramani, Effects of spanwise spacing on large-scale secondary flows in rough-wall turbulent boundary layers, *J. Fluid Mech.* **774** (2015).
- [53] I. Nezu and H. Nakagawa, *Turbulence in Open-Channel Flows* (A. A. Balkema, Brookfield, VT, 1993).
- [54] Z.-Q. Wang and N.-S. Cheng, Secondary flows over artificial bed strips, *Adv. Water Res.* **28**, 441 (2005).
- [55] D. A. Vermaas, W. S. J. Uijttewaai, and A. J. F. Hoitink, Lateral transfer of streamwise momentum caused by a roughness transition across a shallow channel, *Water Resour. Res.* **47**, W02530 (2011).
- [56] H. J. Perkins, The formation of streamwise vorticity in turbulent flow, *J. Fluid Mech.* **44**, 721 (1970).
- [57] F. B. Gessner, The origin of secondary flow in turbulent flow along a corner, *J. Fluid Mech.* **58**, 1 (1973).
- [58] W. Anderson, Q. Li, and E. Bou-Zeid, Numerical simulation of flow over urban-like topographies and evaluation of turbulence temporal attributes, *J. Turbul.* **16**, 809 (2015).
- [59] B. Boashash, Estimating and interpreting the instantaneous frequency of a signal. Part 1: Fundamentals, *Proc. IEEE* **80**, 520 (1992).
- [60] L. Cohen, Time-frequency distributions: A review, *Proc. IEEE* **77**, 941 (1989).
- [61] U. Piomelli, J. Ferziger, P. Moin, and J. Kim, New approximate boundary conditions for large eddy simulations of wall-bounded flows, *Phys. Fluids A* **1**, 1061 (1989).
- [62] J. Albertson and M. Parlange, Surface length scales and shear stress: Implications for land-atmosphere interaction over complex terrain, *Water Resour. Res.* **35**, 2121 (1999).
- [63] F. Porte-Agel, C. Meneveau, and M. B. Parlange, A scale-dependent dynamic model for large-eddy simulation: Application to a neutral atmospheric boundary layer, *J. Fluid Mech.* **415**, 261 (2000).
- [64] W. Anderson and C. Meneveau, A large-eddy simulation model for boundary-layer flow over surfaces with horizontally resolved but vertically unresolved roughness elements, *Boundary-Layer Meteorol.* **137**, 397 (2010).
- [65] W. Anderson, An immersed boundary method wall model for high-Reynolds number channel flow over complex topography, *Int. J. Numer. Methods Fluids* **71**, 1588 (2012).
- [66] E. Bou-Zeid, C. Meneveau, and M. B. Parlange, A scale-dependent lagrangian dynamic model for large eddy simulation of complex turbulent flows, *Phys. Fluids* **17**, 025105 (2005).
- [67] S. Chester, C. Meneveau, and M. B. Parlange, Modelling of turbulent flow over fractal trees with renormalized numerical simulation, *J. Comput. Phys.* **225**, 427 (2007).
- [68] M. Calaf, C. Meneveau, and J. Meyers, Large eddy simulation study of fully developed wind-turbine array boundary layers, *Phys. Fluids* **22**, 015110 (2010).

- [69] M. Calaf, M. B. Parlange, and C. Meneveau, Large eddy simulation study of scalar transport in fully developed wind-turbine array boundary layers, *Phys. Fluids* **23**, 126603 (2011).
- [70] W. Anderson, P. Passalacqua, F. Porté-Agel, and C. Meneveau, Large-eddy simulation of atmospheric boundary layer flow over fluvial-like landscapes using a dynamic roughness model, *Boundary-Layer Meteorol.* **144**, 263 (2012).
- [71] J. Graham and C. Meneveau, Modeling turbulent flow over fractal trees using renormalized numerical simulation: Alternate formulations and numerical experiments, *Phys. Fluids* **24**, 125105 (2012).
- [72] W. Anderson and M. Chamecki, Numerical study of turbulent flow over complex aeolian dune fields: The White Sands National Monument, *Phys. Rev. E* **89**, 013005 (2014).
- [73] R. J. A. M. Stevens, M. Wilczek, and C. Meneveau, Large-eddy simulation study of the logarithmic law for second- and higher-order moments in turbulent wall-bounded flow, *J. Fluid Mech.* **757**, 888 (2014).
- [74] M. Wilczek, R. J. A. M. Stevens, and C. Meneveau, Spatio-temporal spectra in the logarithmic layer of wall turbulence: Large-eddy simulations and simple models, *J. Fluid Mech.* **769**, R1 (2015).
- [75] M. Germano, Turbulence—the filtering approach, *J. Fluid Mech.* **238**, 325 (1992).
- [76] J. S. Smagorinsky, General circulation experiments with the primitive equations, *Mon. Weather Rev.* **91**, 99 (1963).
- [77] N. Hutchins, T. B. Nickels, I. Marusic, and M. S. Chong, Hot-wire spatial resolution issues in wall-bounded turbulence, *J. Fluid Mech.* **635**, 103 (2009).
- [78] I. P. Castro, H. Cheng, and R. Reynolds, Turbulence over urban-type roughness: Deductions from wind-tunnel measurements, *Boundary-Layer Meteorol.* **118**, 109 (2006).
- [79] O. Coceal, A. Dobre, T. G. Thomas, and S. E. Belcher, Structure of turbulent flow over regular arrays of cubical roughness, *J. Fluid Mech.* **589**, 375 (2007).
- [80] Y. Wu and K. T. Christensen, Population trends of spanwise vortices in wall turbulence, *J. Fluid Mech.* **568**, 55 (2006).
- [81] G. M. Fishpool, S. Lardeau, and M. A. Leschziner, Persistent non-homogeneous features in periodic channel-flow simulations, *Flow Turbul. Combust.* **83**, 323 (2009).
- [82] R. T. Reynolds, P. Hayden, I. P. Castro, and A. G. Robins, Spanwise variations in nominally two-dimensional rough-wall boundary layers, *Exp. Fluids* **42**, 311 (2007).
- [83] S. Pope, *Turbulent Flows* (Cambridge University Press, Cambridge, UK, 2000).
- [84] N. Hutchins and I. Marusic, Large-scale influences in near-wall turbulence, *Philos. Trans. R. Soc. A* **365**, 647 (2007).